Math. Model. Nat. Phenom. 21 (2026) 20
https://doi.org/10.1051/mmnp/2026012

**Mathematical Modelling of Natural Phenomena**
www.mmnp-journal.org

# SELF-ORGANIZATION OF PLANKTON PATCHINESS ACROSS MULTIPLE SCALES: AN EXPLANATION COUPLING REACTION–DIFFUSION MODEL AND ENVIRONMENTAL HETEROGENEITY

Tousheng Huang[1,*], Yufei Zhao[1], Xuewei Sun[2], Zhenyu Ren[1], Jincheng Zheng[1], Xingyu Zhou[1], Lele Zhang[1], Wang Tian[1] and Yonglan Tian[1]

**Abstract.** The nonlinear mechanisms underlying the emergence of plankton patchiness have attracted considerable attention in recent decades. In this research, a coupled reaction–diffusion model for phytoplankton-zooplankton interactions is developed by incorporating plankton migration across water layers. Conditions for pattern self-organization are derived through stability analysis, and robustness of multiscale pattern regimes is quantified through local and global sensitivity analyses. When the dispersion relation has multiple peaks, both pure Turing and Hopf–Turing instabilities can generate patterns with two or three coexisting patch sizes. Variance spectrum analysis on the multiscale patterns shows a power-law distribution of plankton variance across spatial scales. Using 1 km as a dividing scale, pure Turing instability mainly shapes smaller-scale patchiness, whereas Hopf–Turing instability has a stronger influence at larger scales. By introducing spatially heterogeneous carrying capacity, the self-organized patterns show variance spectra with slopes comparable to those reported in the literature. Additional tests with nutrient limitation and turbulence demonstrate that multiscale patchiness persists under more realistic forcing, and comparison with chlorophyll-$a$ spectra from the Bohai and Yellow Seas supports the model ability to reproduce scaling behavior. These findings suggest that Turing instability and environmental heterogeneity can jointly provide a plausible mechanism for multiscale plankton patchiness observed in natural ecosystems.

Received May 28, 2025. Accepted April 3, 2026.

## 1. Introduction

The spatiotemporal dynamics and pattern self-organization of plankton in aquatic ecosystems have been a hot topic for a long time. As widely observed and recorded, the plankton often shows nonuniform and discontinuous patchy distribution in space [1–5], and such patchiness characteristics can demonstrate in multiscales [6–8]. Empirical and theoretical research works in recent decades suggest that the reasons and mechanisms for the

*Keywords and phrases:* Plankton patchiness; pattern emergence; Turing instability; reaction–diffusion model; power-law distribution.

[1] Research Center for Engineering Ecology and Nonlinear Science, North China Electric Power University, Beijing 102206, PR China.
[2] Powerchina Beijing Engineering Corporation Limited, Beijing 100024, PR China.

* Corresponding author: tous_huang@ncepu.edu.cn

formation of plankton patchiness are really very complicated [7, 9–11]. Mechanisms related to biotic and abiotic processes have been recognized [10, 12–15]. The biotic mechanisms include reproduction, finding food, mating, vertical migration, predator avoidance, and social behaviors [12, 16], whereas the abiotic factors may be the heterogeneous distributions of oxygen, salinity, temperature and generation of turbulence flow [2, 7, 9–11, 13, 17]. Moreover, since the plankton exhibits different responses to environmental heterogeneity, the interactions between biotic and abiotic processes can cause the occurrence of high complexity of spatial plankton distribution [9–11]. Until now, the research on the plankton dynamics and pattern self-organization still confronts many challenges, and the effects of biological processes at the population level in combination with environmental heterogeneity need further recognition to promote the understanding on the formation of complex plankton patchiness.

As is well recognized, the complex spatial variability of the underlying environment is a basic factor affecting plankton abundance and pattern formation [9, 13, 17, 18]. Since the spatial heterogeneity of environmental conditions plays a key role in influencing the productivity, diversity, and stability of ecosystems, understanding how it controls the occurrence of plankton patterns would be a prerequisite for evaluating the aquatic ecosystem functions [1]. Greer *et al.* detected the formation of plankton patchiness is highly dependent on the heterogeneity of environmental conditions, and especially, oxygen concentration can be a principal driver of patchiness when it reached the threshold of hypoxia [17]. Notably, an important and ubiquitous phenomenon of environmental heterogeneity in aquatic ecosystems is the stratification along vertical depth. It has been recorded that stratification of physical, chemical, and biological components can often take place due to the vertical gradients of temperature, salinity, *etc.*, and lead to inhomogeneous distribution of planktonic organisms [19–23]. Yang *et al.* found that the stratification under frozen lakes in winter can influence subsequent dissolved oxygen concentration in spring and the following temporal dynamics and spatial distribution of plankton [22]. Ríos *et al.* also demonstrated that vertical patches of phytoplankton frequently occur in stable and highly stratified water columns whereas well-mixed waters often display more homogeneous vertical phytoplankton distribution [21].

Nonlinear biological processes occurring on the heterogeneous environment act as a key that determines the plankton pattern characteristics and formation processes [7, 11, 24]. Specifically, when the water column displays multiple layers induced by vertical environmental heterogeneity, the plankton vertical migration between different water layers and the horizontal diffusion of plankton can exert dominant effects in the formation of complex plankton patterns. In the literature, the nonlinear mechanisms related to the effects of plankton mobility have been recognized well [25–31]. Early in the work of Levin and Segel, they first proposed that diffusion-driven instability occurring in the phytoplankton-zooplankton predator-prey interactions can explain the spatial heterogeneity of plankton distribution [25]. Cohen and Shurin also believed that the spatial patterns emerging in the plankton community not only come from environmental heterogeneity, but also are related to the diffusion of plankton [32]. The diffusion-driven instability mechanism has been further applied and achieved good prediction for the patchiness structures of plankton [26, 27, 33, 34]. For the plankton vertical migration, a few approaches demonstrated that it can be regarded as one of the most extensive and strongest reasons for the emergence of plankton patchiness [10–12, 16, 35]. Chen *et al.* performed a model study and found that diel vertical migration can synchronize zooplankton vertical positions with the horizontal current velocities and cause the self-organization of horizontal patchiness [16]. Although considerable progress has been achieved in understanding how plankton vertical migration and horizontal diffusion drive the plankton pattern self-organization, however, the mechanism for how the combination of the two ways of plankton mobility promotes the complexity of plankton patchiness is still poorly known.

Mathematical modeling provides an effective tool for penetrating into the nonlinear mechanisms of plankton pattern formation and quantifying the evolution process and characteristics of plankton patchiness. The theoretical framework established in previous approaches demonstrated that reaction–diffusion model can be employed to describe the ecological processes including growth, mortality, predation, and diffusion of the plankton and to exhibit the plankton pattern formation caused by diffusion-driven instability [25, 27–30, 33, 34]. From the viewpoint of nonlinear dynamics, the pattern formation of plankton systems originates from dynamical instability and is always accompanied by the phenomenon of symmetry breaking. The diffusion-driven instability induced by the difference of plankton mobility causes spatial symmetry breaking; independent upon the space

dimension, the occurrence of bifurcations such as Hopf bifurcation causes temporal symmetry breaking. The co-occurrence of spatial and temporal symmetry breaking is crucial for the generation of plankton pattern complexity [27, 29, 31]. Based on the previous reaction–diffusion model considered for plankton systems, we further introduce the vertical environmental heterogeneity and the vertical migration of plankton between water layers into the model. In this research, the nonlinear mechanism for the emergence of plankton patchiness with multiple patch-sizes is recognized, and we find that the combined effects of Turing instability and environmental heterogeneity can yield patchiness characteristics that are close to natural plankton patterns.

## 2. Model and methods

### 2.1. Spatiotemporal dynamical model

The reaction–diffusion models employed in previous studies for plankton pattern formation are revisited firstly. According to the works of Medvinsky *et al.* [27], Steele and Henderson [33], Brentnall *et al.* [34], Matthews and Brindley [36], Vilar *et al.* [37], an intuitive model proposed to explain plankton dynamics can be described as

$$\frac{\partial P}{\partial t} = f_1(P, Z) + \nabla \cdot (D_1 \nabla P), \tag{2.1a}$$

$$\frac{\partial Z}{\partial t} = f_2(P, Z) + \nabla \cdot (D_2 \nabla Z). \tag{2.1b}$$

The two compartments considered in the model represent the population densities of phytoplankton ($P$) and herbivorous zooplankton ($Z$). Reaction functions $f_1$ and $f_2$ account for the interactions between the phytoplankton and zooplankton populations. $\nabla \cdot (D_1 \nabla P)$ and $\nabla \cdot (D_2 \nabla Z)$ describe the horizontal diffusion of phytoplankton and zooplankton, and $D_1$ and $D_2$ are the diffusion coefficients. The use of model (2.1) is common in theoretical works of ecological pattern formation since it can generate spatial heterogeneous patterns under homogeneous environmental conditions. That is to say, even though the external conditions for the living of plankton are homogeneous, plankton patchiness can still emerge merely due to the interactions and dispersal of the plankton.

It is widely accepted that the prey–predator models are feasible to describe the plankton dynamics since the interaction of phytoplankton and herbivorous zooplankton is essentially a predation relationship. For biological significance, the functions $f_1$ and $f_2$ can have the following structure: $f_1(P, Z) = G(P) - E(P, Z)$, $f_2(P, Z) = \varepsilon E(P, Z) - \eta Z$, where $G(P)$ describes the net growth of the phytoplankton, $E(P, Z)$ describes the predatory interaction between the phytoplankton and the zooplankton, parameter $\varepsilon$ is conversion rate of eaten phytoplankton into new zooplankton abundance, and parameter $\eta$ describes the mortality rate of the zooplankton.

The particular form of functions $G(P)$ and $E(P, Z)$ is dependent on the type of phytoplankton and zooplankton populations and the predatory relationship between them. If it is not the resource-limited case, the classical logistic form can be used to describe the phytoplankton growth, *i.e.*, $G(P) = rP(1-P/K)$, where $r$ is the phytoplankton growth rate and $K$ is the carrying capacity. The expression of $E(P, Z)$ is related to the type of functional response of the predator. As justified and verified by literature [38, 39], in the case of multiple phytoplankton species, an effective and feasible functional response utilized for the plankton dynamics can be described as $E(P, Z) = \beta {P_k}^a Z/(B^a + qZB^a + \sum \omega_k {P_k}^a)$, where parameter $\beta$ is the maximum consumption rate, $P_k$ denotes the $k$th phytoplankton resource consumed by the zooplankton, parameter $a$ regulates the predation functional response from Holling type II ($a = 1$) to Holling type III ($a = 2$), parameter $B$ is a half-saturation constant, parameter $q$ is the predator interference coefficient, and parameter $\omega_k$ is the prey preference of zooplankton for the $k$th phytoplankton (notice $\sum \omega_k = 1$). If we consider the phytoplankton biomass as a whole and set $a = 1$, the functional response can be simplified as $E(P, Z) = \beta PZ/(B + P + wZ)$ with $w = qB$, which is also known as the Beddington-DeAngelis type functional response. This type of functional response is adequate to describe the plankton dynamics in the case of predator interference. Moreover, it can induce complex

spatiotemporal dynamics and rich Turing patterns [40–42] that can help to reveal the outcomes of patterns and mechanisms.

The plankton diffusion is determined by the motility of plankton as well as the turbulent diffusion. This study takes the same consideration as that in Steele and Henderson [33] and Brentnall *et al.* [34]. Although the diffusivity $D_1$ and $D_2$ may vary in space, constant diffusivity for phytoplankton and zooplankton is also considered likewise in previous works and the diffusion term $\nabla \cdot (D_i \nabla)$ can be rewritten as $D_i \nabla^2$. The turbulent diffusion is parameterized by a parameter $\kappa_1$ in a crude but familiar way [34]. The motility of phytoplankton is neglected and the diffusivity $D_1$ takes the value of $\kappa_1$. The diffusivity of zooplankton is considered as $D_2 = \mu_1 \kappa_1$ where $\mu_1$ is the ratio of zooplankton to phytoplankton diffusivity providing a rough and ready method for building zooplankton behavior [34]. When $\mu_1 < 1$, the zooplankton tends to aggregate; when $\mu_1 > 1$, the zooplankton tends to disperse; when $\mu_1 = 1$, the case is that zooplankton is essentially non-motile.

Extending upon the reaction–diffusion model, we additionally factor in the influence of heterogeneous water layers on plankton dynamics. A vertically heterogeneous environment may cause varied plankton dynamics across different water layers. In the aquatic environment, biological exchanges influencing plankton dynamics between water layers are frequently a consequence of plankton motility as well as vertical water flow, such as upwelling and downwelling processes. Generally, the marine water or deep lakes can typically be divided into three layers based on temperature and density differences, *i.e.*, surface layer, thermocline, and bottom layer. The plankton dynamics within each layer can be viewed as distinct subsystems. The dynamics of these subsystems are interconnected through the vertical migration of plankton that effectively couples them together. For modeling purpose, we consider the spatiotemporal dynamics of phytoplankton and zooplankton follows reaction–diffusion equations (2.1) in each layer. We use $P_i$ and $Z_i$ ($i = 1, 2, 3$) to describe the population densities of phytoplankton and zooplankton in the $i$th subsystem.

The parameters for the subsystems in the three layers can be taken differently, illustrating how the inter-layer heterogeneity affects the plankton dynamics of the subsystems. In contrast, identical parameters for the subsystems suggests that the subsystems are mixed very well. For the sake of simplicity, we assume that plankton vertical migration between layers is linearly dependent on the densities of phytoplankton and zooplankton populations. Like the turbulent diffusion, we use $\kappa_2$ to parameterize the migration rate induced by vertical water movement in an average way. Therefore, the vertical migration rate for phytoplankton gives $h_1 = \kappa_2$, and for zooplankton takes $h_2 = \mu_2 \kappa_2$. The value of $\mu_2$ suggests that the zooplankton swim against ($\mu_2 < 1$) or along ($\mu_2 > 1$) the vertical water movement.

The ecological processes described above are sufficiently detailed to sketch the primary features of real planktonic ecosystems in the aquatic environment. Summarizing these description gives the following dynamical equations of a coupled reaction–diffusion model:

$$\frac{\partial P_i}{\partial t} = r_i P_i \left(1 - \frac{P_i}{K_i}\right) - \frac{\beta_i P_i Z_i}{B_i + P_i + w_i Z_i} + h_1 \left(\sum_{j \in \Omega_i} P_j - N_i P_i\right) + D_{1i} \nabla^2 P_i, \tag{2.2a}$$

$$\frac{\partial Z_i}{\partial t} = \frac{\varepsilon_i \beta_i P_i Z_i}{B_i + P_i + w_i Z_i} - \eta_i Z_i + h_2 \left(\sum_{j \in \Omega_i} Z_j - N_i Z_i\right) + D_{2i} \nabla^2 Z_i. \tag{2.2b}$$

The subscript $i$ refers to the $i$th subsystem, $i = 1, 2, 3$. The parameters $h_1$ and $h_2$ are the vertical migration rates of phytoplankton and zooplankton. The symbol $\Omega_i$ denotes the neighborhood subsystem(s) of the $i$th subsystem, and obviously $\Omega_1 = \{2\}$, $\Omega_2 = \{1, 3\}$, and $\Omega_3 = \{2\}$. Correspondingly, $N_i = |\Omega_i|$ is the number of elements in the set $\Omega_i$, and we have $N_1 = 1$, $N_2 = 2$, and $N_3 = 1$.

Notice that three aspects of simplifications are made in the model for the sake of simplifying the complicated situations occurring in the natural aquatic environment. Firstly, since we mainly focus on the heterogeneity between water layers, the plankton dynamics in each layer is considered to take place in a homogeneous environment. Such homogeneity is assumed roughly and only averaged for taking constant parameter values for each subsystem. Secondly, the diffusion of plankton in each stratified layer is simplifiedly considered by the operator $\nabla^2 = \partial^2/\partial x^2 + \partial^2/\partial y^2$ where $x$ and $y$ represent the two dimensions in the horizontal plane. This is reasonable when the horizontal space is much larger than the thickness of the water layers. In such case, averaged vertical homogeneity is considered for the plankton diffusion. Of course, if one stratified layer shows very high vertical heterogeneity, we can totally split this layer into more layers and the total number of subsystems considered in the model becomes higher. Thirdly, the model does not explicitly include the terms of external biological factors such as the effects of nutrients and dissolved oxygen, nutrient recycling, predation of aquatic macroanimals, and so on, since we want to grasp the nonlinear mechanism of plankton pattern formation directly related to the plankton interactions and movement.

## 2.2. Stability analysis

The basic routine of analyzing nonlinear dynamical systems often starts from equilibriums and the stability analysis. Denote one equilibrium of the coupled system (2.2) as ($P_1{}^*$, $Z_1{}^*$, $P_2{}^*$, $Z_2{}^*$, $P_3{}^*$, $Z_3{}^*$). Since the subsystems have different parametric conditions due to vertical heterogeneity, the equilibriums of the coupled system would be very complex, and it is difficult to obtain the analytical equilibrium solutions. Newton method is utilized to numerically solve the equilibriums. Initial conditions of $P$ and $Z$ for iteration in the Newton method are randomly taken from the intervals ($P_{min}$, $P_{max}$) and ($Z_{min}$, $Z_{max}$), respectively, in which $P_{min} = \min(P_{10}, P_{20}, P_{30})$, $P_{max} = P_{10} + P_{20} + P_{30}$, $Z_{min} = \min(Z_{10}, Z_{20}, Z_{30})$, and $Z_{max} = Z_{10} + Z_{20} + Z_{30}$, and ($P_{i0}$, $Z_{i0}$) is the positive interior equilibrium of the $i$th subsystem before the system coupling. A calculation leads to $P_{i0} = \{\eta_i K_i + r_i\varepsilon_i w_i K_i - \varepsilon_i\beta_i K_i + [(\eta_i K_i + r_i\varepsilon_i w_i K_i - \varepsilon_i\beta_i K_i)^2 + 4r_i\varepsilon_i w_i B_i\eta_i K_i]^{1/2}\}/(2r_i\varepsilon_i w_i)$, $Z_{i0} = P_{i0}(\varepsilon_i\beta_i - \eta_i)/(w_i\eta_i) - B_i/w_i$. 10000 initial conditions are taken for iterations to obtain multiple equilibriums possibly existing in the system.

The Jacobian matrix is applied to determine the stability of the equilibriums. The Jacobian matrix associated to the coupled system at any point is calculated as the following:

$$J = \begin{pmatrix} {A_{11}}^{(1)} - h_1 & {A_{12}}^{(1)} & h_1 & 0 & 0 & 0 \\ {A_{21}}^{(1)} & {A_{22}}^{(1)} - h_2 & 0 & h_2 & 0 & 0 \\ h_1 & 0 & {A_{11}}^{(2)} - 2h_1 & {A_{12}}^{(2)} & h_1 & 0 \\ 0 & h_2 & {A_{21}}^{(2)} & {A_{22}}^{(2)} - 2h_2 & 0 & h_2 \\ 0 & 0 & h_1 & 0 & {A_{11}}^{(3)} - h_1 & {A_{12}}^{(3)} \\ 0 & 0 & 0 & h_2 & {A_{21}}^{(3)} & {A_{22}}^{(3)} - h_2 \end{pmatrix}. \tag{2.3}$$

For notational convenience, let $A^{(i)} = [{A_{pq}}^{(i)}]_{2\times 2}$ denote the local Jacobian block of the $i$th subsystem, where $p, q \in \{1, 2\}$, $p = 1$ corresponds to phytoplankton, and $p = 2$ corresponds to zooplankton. The entries of $A^{(i)}$ are given by ${A_{11}}^{(i)}$, ${A_{12}}^{(i)}$, ${A_{21}}^{(i)}$, ${A_{22}}^{(i)}$, with ${A_{11}}^{(i)} = r_i(1-2P_i/K_i) - \beta_i Z_i(B_i+w_i Z_i)/(B_i+P_i+w_i Z_i)^2$, ${A_{12}}^{(i)} = -\beta_i P_i(B_i+P_i)/(B_i+P_i+w_i Z_i)^2$, ${A_{21}}^{(i)} = \varepsilon_i\beta_i Z_i(B_i+w_i Z_i)/(B_i+P_i+w_i Z_i)^2$, ${A_{22}}^{(i)} = \varepsilon_i\beta_i P_i(B_i+P_i)/(B_i+P_i+w_i Z_i)^2 - \eta_i$. Substituting the value of equilibriums into matrix (2.3), and calculating the eigenvalues. Denote the six eigenvalues of matrix (2.3) are $\lambda_1, \lambda_2, \ldots, \lambda_6$, and utilize "Re" and "Im" to represent the functions that take the real part and imaginary part of a complex number, respectively. If $\max(\mathrm{Re}(\lambda_s))$ ($s = 1, \ldots, 6$) is smaller than zero, the equilibrium is locally asymptotically stable; if $\max(\mathrm{Re}(\lambda_s))$ is larger than zero, the equilibrium is asymptotically unstable. Moreover, with the change of system parameter(s), the stability of equilibriums may change, suggesting the occurrence of bifurcation. In this research, the occurrence conditions of Hopf bifurcation are checked since the Hopf bifurcation is crucial for the plankton pattern formation as demonstrated by previous approaches [27, 29, 31]. When the equilibrium has one pair of conjugate complex eigenvalues and the real part of the eigenvalues turn from negative to positive (or vice versa) as system parameter changes,

the Hopf bifurcation may occur. Suppose $\lambda_1$ and $\lambda_2$ are two conjugate complex eigenvalues and select one control parameter such as $h_1$. *Via* $\mathrm{Re}(\lambda_1) = 0$ calculate the critical value $h_1 = h_{1c}$, and simultaneously check $\partial Re\,(\lambda_1)\,/\partial h_1|_{h_1=h_{1c}} \neq 0$, we may find the occurrence of Hopf bifurcation that causes periodic oscillations of the plankton dynamics. Notice this criterion is just necessary, and the strict conditions can refer to the literature [43].

The conditions for plankton pattern formation are determined by Turing instability analysis. According to the standard process, we perform spatially heterogeneous perturbations around the stable equilibrium of the system (2.2), *i.e.*,

$$\begin{pmatrix} P_1 \\ Z_1 \\ P_2 \\ Z_2 \\ P_3 \\ Z_3 \end{pmatrix} = \begin{pmatrix} P_1^* \\ Z_1^* \\ P_2^* \\ Z_2^* \\ P_3^* \\ Z_3^* \end{pmatrix} + \varepsilon \begin{pmatrix} P_{1m} \\ Z_{1m} \\ P_{2m} \\ Z_{2m} \\ P_{3m} \\ Z_{3m} \end{pmatrix} \mathrm{e}^{\lambda t + \hat{\imath}\mathbf{m}\cdot\mathbf{r}} + c.c. + O\left(\varepsilon^2\right), \tag{2.4}$$

where $P_{im}$ and $Z_{im}$ are the amplitudes of the heterogeneous perturbations associated with $P_i$ and $Z_i$, respectively; $\lambda$ describes the temporal growth rate of the perturbations; $\mathbf{r} = (x, y)$ is the horizontal position vector; $\mathbf{m}$ is the wave vector with $\mathbf{m} \cdot \mathbf{m} = m^2$ in which $m$ is the scalar wavenumber; $\hat{\imath}$ is the imaginary unit; and *c.c.* denotes the complex conjugate. Substituting equation (2.4) into system (2.2), then we have the linearized matrix $J_M = J - Dm^2$, where $D = \mathrm{diag}(D_{11}, D_{21}, D_{12}, D_{22}, D_{13}, D_{23})$ and "diag" is a function that generates a diagonal matrix using the elements of a vector.

To write the characteristic polynomial conveniently, we further define ${B_{pp}}^{(i)} = {A_{pp}}^{(i)} - h_p - D_{pi}m^2$ ($i = 1, 3$, $p = 1, 2$), and ${B_{pp}}^{(2.2)} = {A_{pp}}^{(2.2)} - 2h_p - D_{p2}m^2$ ($p = 1, 2$). Also, the index sets $\phi_1 = \{(1, 2, 3), (2, 1, 3), (2, 3, 1), (3, 2, 1)\}$, $\phi_2 = \{(1, 2, 3), (3, 1, 2)\}$, and $\phi_3 = \{(1, 2, 3), (1, 3, 2), (2, 3, 1)\}$ are introduced to abbreviate the permutation terms appearing in the dispersion relation. Then, from $|\lambda - J_M| = 0$, the dispersion relation determining the onset of pattern formation can be written as follows:

$$\begin{aligned}
&\textstyle\prod_{i=1}^{3}\prod_{p=1}^{2}\left(\lambda - B_{pp}^{(i)}\right) - \sum_{p,q=1,2}^{p\neq q}\sum_{i=1,3}\left(h_p^2\left(\lambda - B_{pp}^{(i)}\right)\prod_{j=1}^{3}\left(\lambda - B_{qq}^{(j)}\right)\right) \\
&-\sum_{i=1}^{3}\left(A_{12}^{(i)}A_{21}^{(i)}\prod_{j=1,j\neq i}^{3}\prod_{p=1}^{2}\left(\lambda - B_{pp}^{(j)}\right)\right) + \sum_{i,j=1,3} h_1^2h_2^2\left(\lambda - B_{11}^{(i)}\right)\left(\lambda - B_{22}^{(j)}\right) \\
&-\sum_{(i,j,k)\in\phi_1} h_1h_2A_{12}^{(i)}A_{21}^{(j)}\prod_{p=1}^{2}\left(\lambda - B_{pp}^{(k)}\right) + \sum_{p,q=1,2}^{p\neq q}\left(h_p^2\sum_{(i,j,k)\in\phi_2} A_{12}^{(i)}A_{21}^{(i)}\left(\lambda - B_{qq}^{(j)}\right)\left(\lambda - B_{qq}^{(k)}\right)\right) \\
&\sum_{(i,j,k)\in\phi_3} A_{12}^{(i)}A_{21}^{(i)}A_{12}^{(j)}A_{21}^{(j)}\prod_{p=1}^{2}\left(\lambda - B_{pp}^{(k)}\right) - h_1^2h_2^2\prod_{p,q=1,2}^{p\neq q}\left(A_{pq}^{(1)} + A_{pq}^{(3)}\right) \\
&\sum_{(i,j,k)\in\phi_2} h_1h_2A_{12}^{(i)}A_{21}^{(i)}\left(A_{12}^{(j)}A_{21}^{(k)} + A_{21}^{(j)}A_{12}^{(k)}\right) - \prod_{i=1}^{3}A_{12}^{(i)}A_{21}^{(i)} = 0.
\end{aligned} \tag{2.5}$$

Equation (2.5) describes how the eigenvalues of linearized matrix $J_M$ change with the wavenumber $m$. Solving equation (2.5) yields six eigenvalue branches $\lambda_s(m)$ ($s = 1, \ldots, 6$). We define the dominant growth rate as $\lambda_d = \max_{m,\,s}\left(Re\left(\lambda_s(m)\right)\right)$. The condition $\lambda_d = 0$ determines the critical threshold for pattern emergence in the coupled system (2.2). When $\lambda_d < 0$, the coupled system attracts back to the homogeneous state ($P_1{}^*$, $Z_1{}^*$, $P_2{}^*$, $Z_2{}^*$, $P_3{}^*$, $Z_3{}^*$) under heterogeneous perturbations. When $\lambda_d > 0$, the coupled system undergoes spatial symmetry breaking and produces heterogeneous patterns. Moreover, $\lambda_d > 0$ in combination with the occurrence of Hopf bifurcation can lead to the Hopf–Turing instability and the emergence of spatiotemporal patterns.

The pattern formation of the coupled system is much more complex than the single system since the dispersion relation may show multiple peaks which suggest the patterns generated by the coupled system can hold different critical Turing modes and thus exhibit the characteristics of nestedness [29, 30]. Here, we follow the steps given in previous research to find the complex patterns of the coupled system [30]. Firstly, Turing pattern selection and Hopf bifurcation of the subsystem is studied, pinpointing the self-organization of cold and hot hexagon, stripe, hexagon-stripe, and spiral patterns in the parameter space. Secondly, adjusting the wavenumbers of the critical Turing modes to find the patterns in which the plankton patches display different sizes or nested structures. The pattern selection of the subsystem can be analyzed by deducing amplitude equations through standard multiscale analysis and has been studied very well in former research works [41, 42]. Therefore, we here just give the results of amplitude equations and the corresponding pattern selection:

$$\varsigma\frac{\partial\varphi}{\partial t}=-\gamma\frac{\rho_1^2\rho_2^2+\rho_1^2\rho_3^2+\rho_2^2\rho_3^2}{\rho_1\rho_2\rho_3}\sin\varphi, \tag{2.6a}$$

$$\varsigma\frac{\partial\rho_1}{\partial t}=\mu\rho_1+\gamma\rho_2\rho_3\cos\varphi-g_1\rho_1^3-g_2\left(\rho_2^2+\rho_3^2\right)\rho_1, \tag{2.6b}$$

$$\varsigma\frac{\partial\rho_2}{\partial t}=\mu\rho_2+\gamma\rho_1\rho_3\cos\varphi-g_1\rho_2^3-g_2\left(\rho_1^2+\rho_3^2\right)\rho_2, \tag{2.6c}$$

$$\varsigma\frac{\partial\rho_3}{\partial t}=\mu\rho_3+\gamma\rho_1\rho_2\cos\varphi-g_1\rho_3^3-g_2\left(\rho_1^2+\rho_2^2\right)\rho_3, \tag{2.6d}$$

which has solutions: (i) stationary state, given by $\rho_1=\rho_2=\rho_3=0$, stable for $\mu<\mu_2=0$ and unstable for $\mu>\mu_2$; (ii) stripe pattern, given by $\rho_1=\sqrt{\mu/g_1}\neq 0$, $\rho_2=\rho_3=0$, stable for $\mu>\mu_3=\gamma^2 g_1\Big/(g_1-g_2)^2$ and unstable for $\mu<\mu_3$; (iii) cold and hot hexagon patterns, given by $\rho_1^{\pm}=\rho_2^{\pm}=\rho_3^{\pm}=\left(|\gamma|\pm\sqrt{\gamma^2+4(g_1+2g_2)\mu}\right)\Big/(2g_1+4g_2)$ with $\varphi=0$ or $\pi$ existing when $\mu>\mu_1=-\gamma^2\Big/(4g_1+8g_2)$, in which $\rho^+$ is stable only for$\mu<\mu_4=\gamma^2(2g_1+g_2)\Big/(g_1-g_2)^2$, and $\rho^-$ is always unstable; and (iv) mixed states, given by $\rho_1=|\gamma|/(g_2-g_1)$,$\rho_2=\rho_3=\sqrt{(\mu-g_1\rho_1^2)/(g_1+g_2)}$ with $g_2>g_1$ and $\mu>g_1\rho_1^2$, in which $\rho$ is always unstable.

## 2.3. Pattern simulation and analysis methods

Based on the theoretical analysis above, we numerically integrate the coupled system to generate plankton patterns. The parameter values used in simulations are selected within the ecologically plausible and empirically motivated ranges summarized in Table 1, which are consistent with established parameterizations in plankton reaction–diffusion modeling studies [26, 27, 29, 33, 34, 44]. Time is measured in days and horizontal distance in hectometers to match characteristic biological timescales and observed patch scales [33]. For each simulation, the specific parameter set is restricted to satisfy the derived theoretical instability conditions.

The coupled system (2.2) is numerically solved on a uniform Cartesian grid in the horizontal plane. For each state variable $u\in\{P_i,\ Z_i\}$, the Laplacian term $\nabla^2 u$ is discretized by the standard five-point, second-order central-difference stencil, *i.e.*, $(\nabla^2 u)_{j,k}\approx(u_{j+1,k}-2u_{j,k}+u_{j-1,k})/{\delta_x}^2+(u_{j,k+1}-2u_{j,k}+u_{j,k-1})/{\delta_y}^2$. Time integration is carried out using an explicit fourth-order Runge-Kutta time-stepping method with $\delta_t$=0.01 day and $\delta_x=\delta_y=1$ hm. Pattern evolution simulations are initialized by adding small random perturbations to the stable homogeneous equilibrium, and zero-flux boundary conditions are imposed for all state variables, *i.e.*, $\partial u/\partial\boldsymbol{n}$=0 on the domain boundary. The stability and convergence properties of the adopted explicit finite-difference/Runge-Kutta discretization are described below.

- Stability. Since the diffusion terms are treated explicitly, the time step is chosen to satisfy a standard diffusion CFL-type stability constraint for two-dimensional reaction–diffusion discretization, *i.e.*,

$|D_{ij}\delta_t(1/{\delta_x}^2+1/{\delta_y}^2)| < 1/2$, for every diffusion coefficient $D_{ij}$ in the system [45, 46]. Using the parameter ranges in Table 1, the maximum diffusivity is $D_{max}$=10 hm$^2$ day$^{-1}$, and thus we have the bound $D_{max}\delta_t(1/{\delta_x}^2+1/{\delta_y}^2) \leq 10\times0.01\times(1+1)=0.2<0.5$, which ensures stable numerical integration of the diffusive transport for all variables and layers. The vertical migration coupling terms are integrated with the same Runge-Kutta step and remain non-stiff under our settings due to $h\delta_t<10^{-3}$.

- Convergence. The spatial discretization is second-order accurate due to the central-difference Laplacian, while the time integration achieves fourth-order from the accuracy of the adopted Runge-Kutta scheme. Hence, the method is consistent with the continuous reaction–diffusion system. Together with the above conditional stability bound for the explicit diffusion update, this yields a convergent approximation for the reaction–diffusion operator under the smooth-solution regime relevant to our simulations.

To quantify how uncertainty in key parameters reshapes the system's pattern state regimes, both local and global sensitivity analyses are performed. Locally, we perturb each parameter one at a time within a prescribed relative range around its baseline value (*i.e.*, for an arbitrary parameter $\varphi$, $\Delta\varphi/\varphi_0=(\varphi-\varphi_0)/\varphi_0\in(-1,\ 2]$), while keeping all other parameters fixed. For each perturbed value, we evaluate the regime classification from the dispersion relation using the unchanged "multiscale pattern" decision rules, and record the largest negative and positive deviations that still remain within the "multiscale pattern" set.

The global sensitivity of multiscale pattern emergence to mobility parameters is quantified using a variance-based Sobol' method. The uncertain input vector consists of eight mobility parameters, ($D_{11}$, $D_{12}$, $D_{13}$, $D_{21}$, $D_{22}$, $D_{23}$, $h_1$, $h_2$), sampled independently within the ranges in Table 1, with diffusion coefficients sampled log-uniformly to account for their multi-order-of-magnitude variability and vertical exchange rates sampled uniformly. We define a binary multiscale indicator $Y$ based on the dispersion curve geometry, setting $Y=1$ when (i) the dominant growth rate $\lambda_d$ over $m>0$ was positive and (ii) the dispersion relation exhibited more than one local maximum, and $Y=0$ otherwise. Sobol' first-order indices $S_i$ and total-effect indices $S_{Ti}$ are estimated from Saltelli sampling with base size $N=10^6$, and second-order interaction indices $S_{ij}$ are computed to quantify pairwise non-additive effects between mobility parameters. Uncertainty in the estimated indices is assessed *via* nonparametric bootstrap resampling, and for the interaction analysis we retain only pairwise effects whose 95% bootstrap confidence interval lower bound exceeded zero, ensuring that reported interactions are robustly positive.

The characteristics of plankton patterns are quantified using variance spectrum analysis, after the transient time of pattern evolution is truncated. For each snapshot, we extract one-dimensional transects from the phytoplankton pattern. Each transect is demeaned and transformed by a discrete Fourier transform to obtain the power spectrum, and spectra from all transects are averaged to yield a representative variance spectrum. We plot log10(variance) against log10(wavenumber) and perform linear regression over a prescribed scale band to estimate the spectral slope $\gamma$. The mean and standard deviation of $\gamma$ across transects are also reported.

## 3. Results

### 3.1. Basic mechanisms: emergence of patterns with multiple patch-sizes

For reaction–diffusion systems, it is well-known that the Turing instability mechanism can result to the formation of heterogeneous patterns. Nevertheless, the plankton patchiness as observed in natural ecosystems often demonstrates very complex characteristics, one of which is the coexistence of plankton patches of multiple sizes. Based on the analysis on the dispersion relation and pattern formation of system (2.2), we find that when Turing instability occurs, the number of peaks on the dispersion relation determines the emergence of patterns with $n$ sizes of plankton patches. Ecologically, each dispersion peak corresponds to a preferred spatial wavelength selected by the balance between local trophic interactions (*e.g.*, growth–grazing feedback) and dispersal, and multiple comparable peaks therefore imply the coexistence of multiple characteristic patch scales within the same community. When $n > 1$, the pattern is also referred to as $n$-patch-size pattern briefly in the following; when $n = 1$, we mention the pattern as regular pattern. Figure 1 exhibits two cases of patterns where $n$-size plankton patches spontaneously take place under the mechanism of pure Turing instability. In the case of Figure

TABLE 1. Ecological explanation of the symbols and reference ranges for the parameters utilized in the coupled system (2.2).

| Symbol* | Ecological meaning | Unit | Range used | Empirical/biological basis |
|---|---|---|---|---|
| $P_i$ | Phytoplankton density (chlorophyll-based proxy) | mg $m^{-3}$ | – | State variable of prognostic chlorophyll-$a$ concentration solved by the model. Its magnitude is widely observed to be patchy in marine environments [2, 4, 5]. |
| $Z_i$ | Herbivorous zooplankton density (wet-weight biomass proxy) | g $m^{-3}$ | – | State variable of prognostic herbivorous zooplankton biomass solved by the model. Its spatial patchiness is closely related to the phytoplankton. |
| $t$ | Time variable | day | – | Time is measured in days to match the characteristic biological timescales of phytoplankton growth and grazing interactions. The daily scaling is consistent with plankton patchiness and reaction–diffusion modeling studies [33, 34, 36]. |
| $x$, $y$ | Space variables in horizontal plane | hm | – | Space is set in hectometers because the model targets sub-kilometer to multi-kilometer patch structures. Using hectometers is consistent with prior plankton patchiness studies that resolve spatial variability over $10^2$–$10^5$ m ranges [2, 33, 34] while keeping diffusion coefficients and grid spacing numerically convenient. |
| $r_i$ | Phytoplankton growth rate | $day^{-1}$ | (0, 1) | Field syntheses of dilution experiments report mean phytoplankton growth rates typically below $1d^{-1}$ across open-ocean to estuarine systems, supporting the used range for realized net growth under natural limitation [47]. Temperature-based maximum-growth envelopes can exceed $1d^{-1}$ in optimal conditions [48, 49], so the range here is interpreted as a conservative realized net rate rather than a physiological upper bound. |
| $K_i$ | Environmental carrying capacity for phytoplankton (chlorophyll-equivalent) | mg $m^{-3}$ | [5, 15] | Observed chlorophyll-$a$ concentrations in productive coastal/temperate/estuarine habitats reach several to >10 $\mu$g $L^{-1}$, with mean values around 5.18 $\mu$g $L^{-1}$ (temperate) and 13.0 $\mu$g $L^{-1}$ (estuarine) reported in a global dilution-experiment synthesis [47], which brackets 5–15 mg $m^{-3}$ as a realistic upper biomass scale for productive patches. |
| $\beta_i$ | Maximum capture/ingestion rate per zooplankton biomass | mg $g^{-1}$ $day^{-1}$ | [0.1, 1] | Empirical grazing parameterizations from dilution data yield maximum specific grazing rates on the order of ∼0.5–1.2 $d^{-1}$ and typical grazing-mortality coefficients on phytoplankton of ∼0.39–0.53 $d^{-1}$ across habitats, indicating that "order-one per day" feeding intensities are common for planktonic consumers [47, 50]. Since $\beta$ is expressed in the model's mixed currency (chlorophyll-$a$ prey units and wet-weight predator units), the range [0.1, 1] mg $g^{-1}$ $d^{-1}$ is chosen to span moderate-to-high feeding intensities consistent with those empirically estimated daily-scale grazing rates after unit mapping. |

TABLE 1. continued.

| Symbol* | Ecological meaning | Unit | Range used | Empirical/biological basis |
|---|---|---|---|---|
| $B_i$ | Half-saturation constant in grazing functional response | mg $m^{-3}$ | [0.1, 2) | Bootstrapped fits of saturating grazing models report half-saturation constants (for prey biomass expressed in nutrient currency) spanning on the order of 0.01–1 $\mu$M in dilution-based parameterizations, which provides an empirical scale for "half-saturation" prey levels [50]. Converting this biomass half-saturation scale to chlorophyll-$a$ using Redfield stoichiometry and typical carbon:chlorophyll ranges yields half-saturation concentrations on the order of ∼0.1–2 mg Chl $m^{-3}$ [48, 50]. This range is also consistent with typical chlorophyll-$a$ levels encountered in oceanic-to-coastal habitats [47]. |
| $w_i$ | Predator interference coefficient | mg $g^{-1}$ | [0, 1] | Predator interference is routinely represented with Beddington–DeAngelis functional responses, and published plankton predator-prey models use this structure to explore regimes from no interference to strong interference [40, 41]. Because direct empirical estimates of $w$ in the specific unit system used here are scarce, we span the range [0,1] mg $g^{-1}$ to cover the full continuum from absent interference to moderate interference effects at the zooplankton biomass levels considered [51]. |
| $\varepsilon_i$ | Conversion rate of ingested phytoplankton into zooplankton biomass | g $mg^{-1}$ | (0, 1) | Zooplankton gross growth efficiencies are commonly reported around ∼0.2–0.3 across taxa in literature, and assimilation and growth efficiencies for zooplankton functional groups have been reported in the approximate ranges 0.33–0.69 and 0.10–0.41, respectively, indicating that biologically plausible efficiencies are well below 1 in most cases [52–54]. We therefore constrain $\varepsilon$ to (0,1) by mass conservation, which is given to include uncertainty introduced by the taxon/environmental variability. |
| $\eta_i$ | Zooplankton mortality rate | $day^{-1}$ | [0.01, 0.5] | Global analyses of in situ copepod mortality indicate typical adult mortality rates on the range of ∼0.06–0.19 $d^{-1}$ across 5–25°C, with higher values up to 0.66 $d^{-1}$ reported under warm estuarine conditions [55], supporting the given range of $\eta$. |
| $D_{1i}$ | Horizontal diffusion coefficient for phytoplankton | $hm^2$ $day^{-1}$ | [0.0001, 1] | Dye-release based diffusion diagrams report horizontal apparent diffusivities spanning ∼$4.1 \times 10^2$ $cm^2$ $s^{-1}$ at 100 m scales to ∼$5.8 \times 10^3$ $cm^2$ $s^{-1}$ at the 1 km scale (≈0.35 to ≈5 $hm^2$ $d^{-1}$ [56]. The given range targets low diffusivity with the consideration of that the phytoplankton taxa often have negligible active motility. |

TABLE 1. continued.

| Symbol* | Ecological meaning | Unit | Range used | Empirical/biological basis |
|---|---|---|---|---|
| $D_{2i}$ | Horizontal diffusion coefficient for zooplankton | $hm^2\ day^{-1}$ | [0.0001, 10] | Unlike phytoplankton, zooplankton can actively swim and can partially resist or adjust to ambient flow. Therefore, their effective horizontal dispersion can deviate substantially from passive-tracer mixing and is represented with a broader exploratory range, which allows weak dispersal or aggregation and strong dispersal regimes [12, 34]. |
| $h_1$ | Vertical migration/exchange rate for phytoplankton | $day^{-1}$ | [0.01, 0.1] | Microstructure observations during restratification report diapycnal diffusivities of order $\sim 5\times10^{-6}$ to $10^{-4}$ $m^2\ s^{-1}$ [57], which correspond to exchange rates $\sim$0.004–0.086 $d^{-1}$ for a 10 m exchange length scale. We thus choose the $h_1$ range here as a physically plausible vertical exchange rate between an upper and a lower layer. |
| $h_2$ | Vertical migration/exchange rate for zooplankton | $day^{-1}$ | [0.01, 0.1] | The same order-of-magnitude diapycnal diffusivity constraints justify using $h_2$ in the same interval as $h_1$, because both patches represent water-column layers subject to comparable ranges of mixing-driven vertical exchange in coastal/ocean shelf settings. |

*: the subscript $i$ in the parameters means the $i$th water layer.

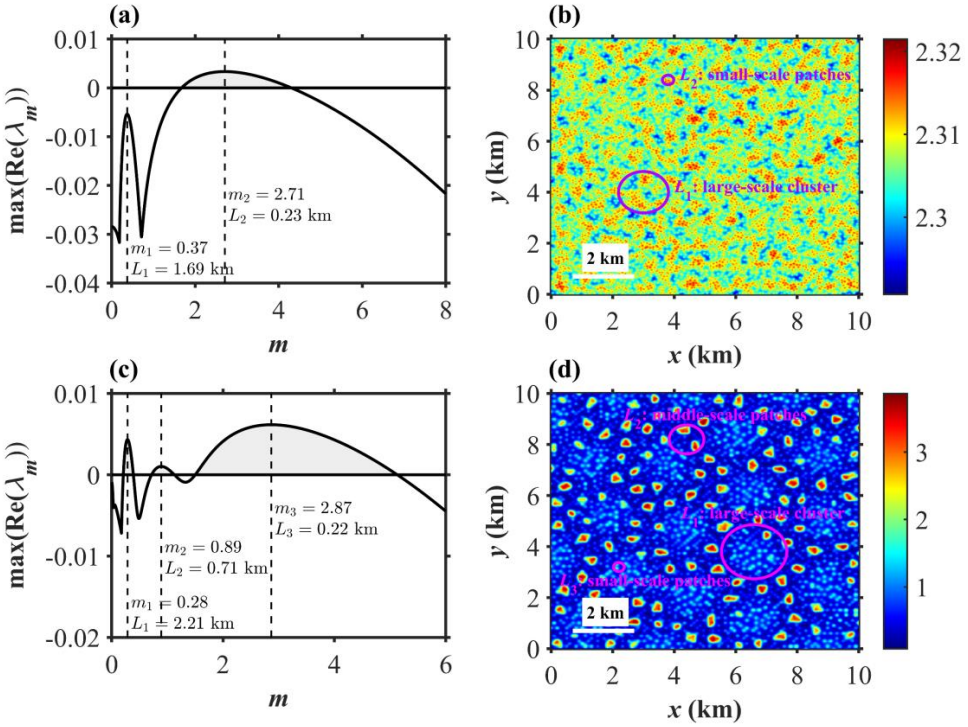


FIGURE 1. Pure Turing instability generates multiscale phytoplankton patchiness. (a, c) Dispersion relation versus wavenumber $m$, where the dashed lines mark the critical Turing modes and the corresponding patch sizes $L_i = 0.2\pi/m_i$ (km). (b, d) Representative snapshots of phytoplankton density after removing transients, with $P_1$ in (b) and $P_2$ in (d), showing two- and three-scale patch structures, where circles highlight patches at scales $L_i$ (scale bar: 2 km). Parameter values are given in Table S1 in the supplementary material.

1a and b, the pattern is composed of two-size patches, and the smaller spot patches are embedded into the larger stripe patches which play a role as the background. In the case of Figure 1c and d, three-size patches are present: the smallest patches occurring as cluster are nested in each largest patch, and the middle-size patches exist in the gap between the largest patches. The pattern formation in Figure 1 displays two ways for the emergence of $n$-size patches, nested and parallel. Generally, the nested structures often take place when the sizes of patches show large difference, with the ratio of smaller patch size to larger one at least less than 1/2.

Hopf instability has an important influence on the generation of irregular or spiral wave patches in the reaction–diffusion system. Here, under the effect of plankton vertical migration, the patterns can further exhibit new characteristics of $n$-size patches. As shown in Figure 2, two cases of such patterns are demonstrated, where small cold or hot spots are nested in the large irregular patches. Also, the key for the emergence of such patterns needs more than one peak on the dispersion relation (Fig. 2a and 2c). It can be found that the sizes for the two types of patches which combine to show nested characteristics have very large difference, suggesting that the Hopf–Turing instability can simultaneously shape the spatial distribution of plankton at different scales (Fig. 2b and 2d). From an ecological perspective, the Hopf component represents intrinsic temporal oscillations of the local trophic system, while the Turing component sets spatial segregation. Their coupling thus naturally yields spatiotemporal patchiness with multiple coexisting spatial scales. This capability of shaping plankton patterns can be explained by a mechanism we proposed previously, "projection of characteristics" that the pattern characteristics of one or more subsystems project into another subsystem and thus the dynamical characteristics of these subsystems combine to form very complex patterns [29]. The mechanism "projection of characteristics",

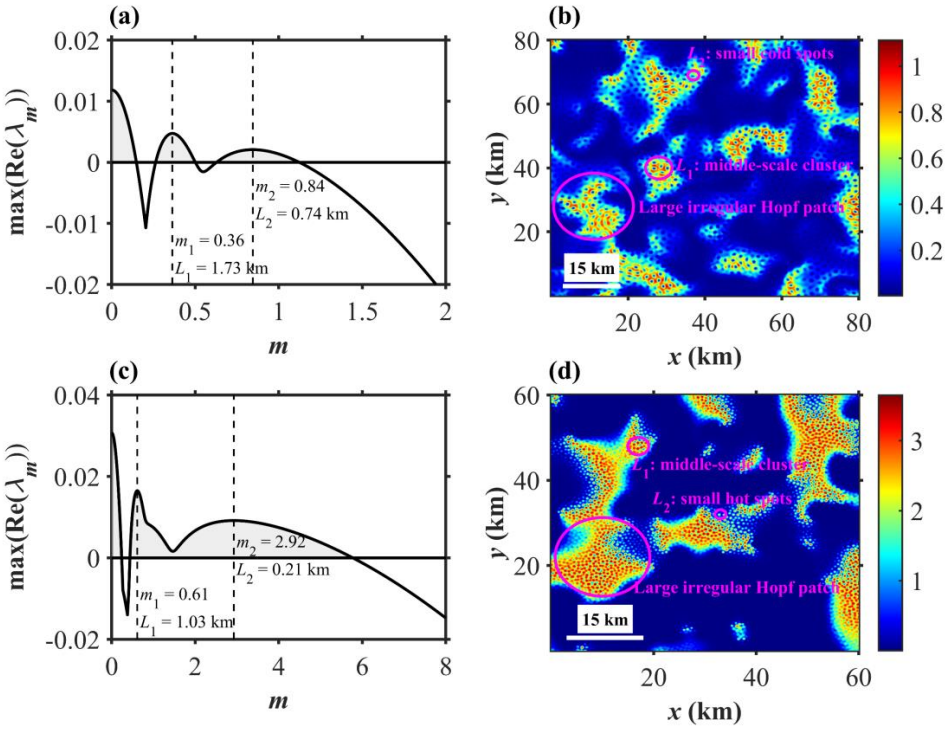


FIGURE 2. Hopf–Turing instability generates nested irregular phytoplankton patchiness. (a, c) Dispersion relation versus wavenumber $m$, where the dashed lines mark the critical Turing modes and the corresponding patch sizes $L_i = 0.2\pi/m_i$ (km). (b, d) Representative snapshots of phytoplankton density $P_1$ after transients are removed, showing small cold/hot spots ($L_2$) and a middle-scale cluster ($L_1$) embedded within a large irregular Hopf patch, with circles highlighting the annotated structures (scale bar: 15 km). Parameter values are given in Table S1 in the supplementary material.

which is induced by plankton vertical migration, synthesizes pattern characteristics from different subsystems and causes the formation of $n$-size patches and even multiscale structures. Meanwhile, the patches at different scales can form in independent processes and then merge into new nestedness structures. In practice, this means that vertical migration can act as an ecological "coupler" across layers, allowing spatial/temporal signatures generated in one layer to imprint onto another layer and thereby enrich the observable patch-size spectrum.

The pure Turing instability and Hopf–Turing instability provide the basic mechanisms for the pattern formation of system (2.2), whereas the number of peaks on the dispersion relation determines the complexity of subtle pattern structures. The combination of the two aspects leads to the outcomes of pattern self-organization with $n$-size patches. For clarity in the following figures, we summarize the dynamical outcomes into discrete regimes and use the same regime definitions, so that parameter sweeps can be interpreted as transitions among regimes rather than as disconnected examples. With the consideration of parameter variations in system (2.2), the parametric space can be divided into six state areas for the existence of various system states: I, homogeneous stationary state (HSS); II, homogeneous oscillating state (HOS) induced by Hopf instability; III, regular Turing pattern (RTP) induced by pure Turing instability; IV, multiscale Turing pattern (MSTP) with $n$-size patches induced by pure Turing instability; V, regular Hopf–Turing pattern (RHTP) induced by the Hopf–Turing instability; VI, multiscale Hopf-Turing pattern (MSHTP) with $n$-size patches induced by the Hopf–Turing instability. Ecologically, areas I–II correspond to spatial homogenization, whereas areas III–VI correspond to spatially structured patchiness, with areas IV and VI specifically capturing multiscale patch-size coexistence.

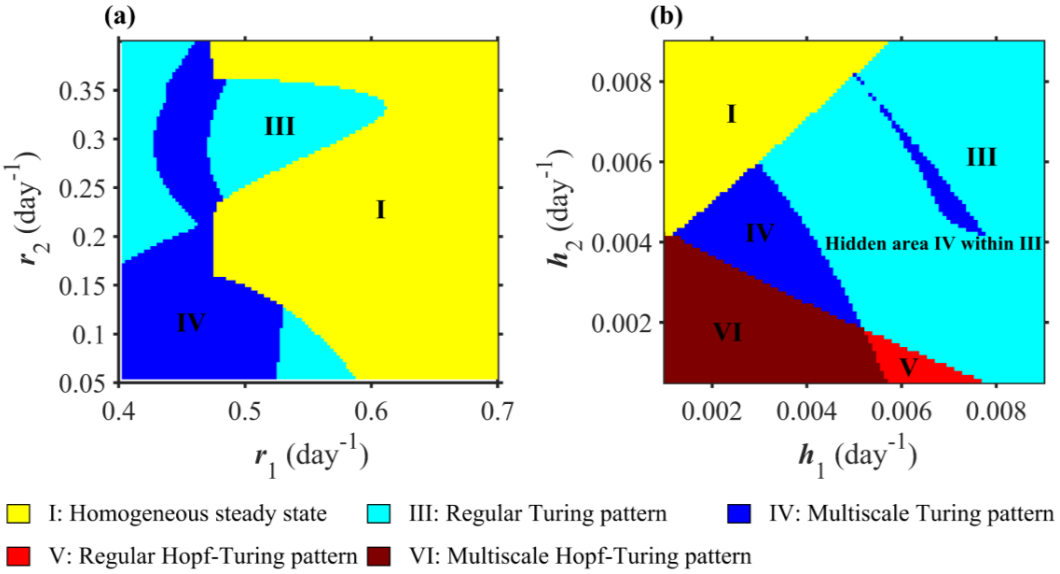


FIGURE 3. State distribution maps in (a) $r_1$-$r_2$ and (b) $h_1$-$h_2$ parameter spaces. Colors indicate dynamical regimes: I (homogeneous steady state), III (regular Turing pattern), IV (multiscale Turing pattern), V (regular Hopf–Turing pattern), and VI (multiscale Hopf–Turing pattern). The parametric conditions for panels (a) and (b) are the same as those in Figures 1a and 2a, respectively.

Figure 3 shows the distribution of the divided state areas in the $r_1$-$r_2$ and $h_1$-$h_2$ parameter spaces for instance. It can be found that the patterns with $n$-size patches distribute in lower $r_1$, $r_2$ and smaller vertical migration rates. Interpreting these parameters ecologically, smaller $r_1$ and $r_2$ indicate weaker net phytoplankton growth (*e.g.*, due to resource or light limitation), while smaller vertical migration rates imply weaker inter-layer exchange (possible due to stronger stratification or reduced motility). Under these conditions, multiple unstable spatial modes can coexist more readily, making multiscale patchiness more likely. The distribution in $r_1$-$r_2$ parameter space implies that state transitions can take place between discrete state areas under the variation of parameters (Fig. 3a). Also, note that in Figure 3b the state area IV is hidden in the area III and can hardly be identified analytically, suggesting that the state distribution can be underestimated. This "hidden" pocket indicates that multiscale patchiness may occur in narrow parameter windows; hence coarse parameter scans (or regime boundaries inferred without sufficient resolution) can miss ecologically relevant but small regions where multiscale patterns emerge.

### 3.2. Complex regime transitions: influence of parameter variation

How the variation of system parameters influences the pattern dynamics is then studied in detail. We sweep the system parameters based on the four cases in Figures 1 and 2, and the results are then demonstrated. These parameter sweeps provide an interpretable link between ecological rates/transport processes and the persistence and complexity of plankton patchiness. For the case of pure Turing instability (Figs. 4 and S1), the sizes of patches can be calculated by the wavenumbers corresponding to the peaks on the dispersion relation. Let the wavenumber determined by a peak be $m_i$, and then the wavelength of the corresponding patch is $0.2\pi/m_i$ km. This calculation can be verified by the dispersion relation and patch sizes in Figure 1.

Different parameter variations exert distinct effects on the system dynamics. In the case of Figure 4, lower phytoplankton growth rates are more likely to cause the emergence of $n$-patch-size patterns. The increase of $r_1$ leads to the system dynamics experiencing four changes: three-patch-size patterns occur at 0.223, and after

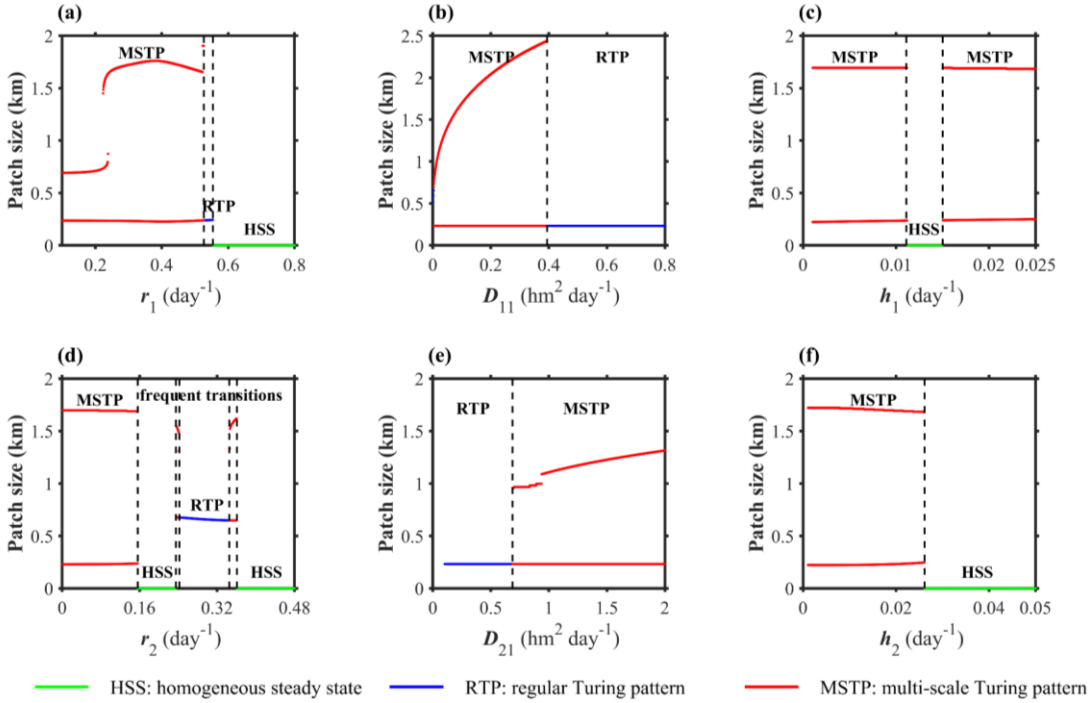


FIGURE 4. Parameter-driven transitions in pattern state and patch sizes for the pure Turing case. Patch sizes (km) are shown as a function of (a) $r_1$, (b) $D_{11}$, (c) $h_1$, (d) $r_2$, (e) $D_{21}$, and (f) $h_2$, with all other parameters fixed to the baseline case in Figure 1b. Colors denote regimes: HSS (green), RTP (blue), and MSTP (red). Vertical dashed lines indicate regime boundaries.

a narrow band of such patterns, the system state changes to the two-patch-size patterns at 0.238, and then suddenly jumps to RTP and HSS at 0.527 and 0.554, respectively (Fig. 4a). This result shows the balance effect of local reactions in the diffusion-driven plankton patchiness. More complex response of system dynamics to the increase of $r_2$ is observed (Fig. 4d), and the frequent changes of system states when $r_2$ crosses 0.156 coincide with the discrete distribution of state areas as described in Figure 3.

Changes in the diffusion coefficients $D_{11}$ and $D_{21}$ take the system dynamics transit between $n$-patch-size patterns and regular Turing patterns (Fig. 4b and 4e). Increasing the two parameters leads to just opposite transitional trend, and this may result from that larger zooplankton diffusion rate and smaller phytoplankton diffusion rate both have ability to shape larger-size patches in the two-patch-size patterns. This opposite trend highlights the classical role of differential mobility between trophic levels in diffusion-driven instability and plankton patchiness models. The change of $h_1$ and $h_2$ brings the transition between two-patch-size patterns and HSS (Fig. 4c and 4f). It is naturally inferred that the increase of vertical migration rates can result to the synchronization of dynamics between water layers. Although in some situations this is right (Fig. 4f), however, the system dynamics can be very complex. Generally, stronger vertical coupling can promote inter-layer synchronization and suppress spatial contrasts, but the response can be nonmonotonic because intermediate exchange may homogenize the layers while larger exchange can also modify the effective instability conditions and re-enable spatial patterning. Likewise, we can quantitatively determine the change of system states and patch sizes with the variation of parameters for the case of Figure 1b, as shown in Figure S1.

For the case of Hopf–Turing instability (Figs. 5 and S2), the sizes of the irregular or spiral wave patches are difficult to analytically calculate. Here, we turn to use dispersion-relation peaks ($\text{Peak}_{dr}$), which is a set including $\max(\lambda_s(0))$ and all peak values on the dispersion relation, to describe the change of system dynamics. In such

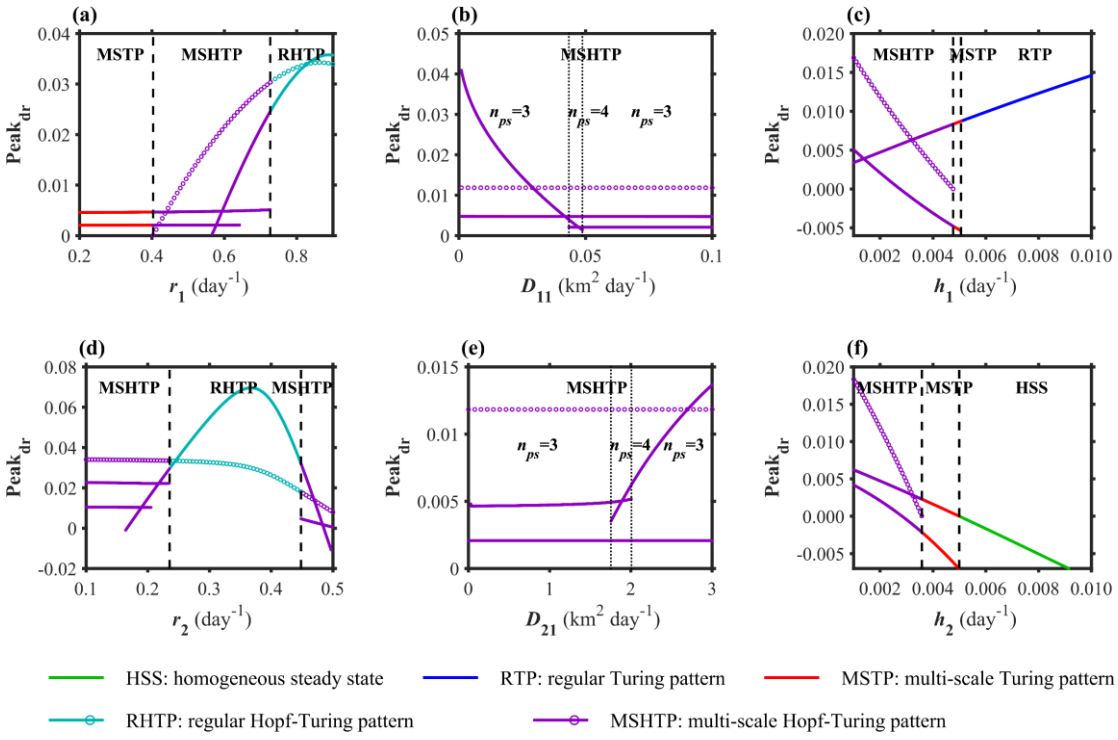


FIGURE 5. Parameter-driven transitions in pattern state for the Hopf–Turing case revealed by dispersion-relation peaks (Peak$_{dr}$), which is plotted versus (a) $r_1$, (b) $D_{11}$, (c) $h_1$, (d) $r_2$, (e) $D_{21}$, and (f) $h_2$, with all other parameters fixed to the baseline case in Figure 2b. Colors/markers denote regimes (see legend), and open circles indicate Hopf-related peaks. Vertical dashed lines mark regime boundaries. In panels (b) and (e) with only a single regime scanned, we use vertical dotted lines to subdivide that regime by the number of coexisting patch-size branches ($n_{pz}$).

case, the parameter sweeps indicate that changes in growth and vertical migration can switch on/off the Hopf component and thereby reorganize the pattern type and the number of coexisting patch-size branches. As shown in Figure 5, increase of $r_1$ and decrease of $h_1$ and $h_2$ can trigger the occurrence of Hopf bifurcation (Fig. 5a, 5c, and 5f), and thus lead to a transition between $n$-patch-size patterns induced by pure Turing or Hopf–Turing mechanisms, respectively. Variation of parameters $D_{11}$ and $D_{21}$ has no effect on the Hopf instability and has minimal impact on the pattern structure (Fig. 5b and 5e). The number of patch sizes can be reduced to one (Fig. 5a, 5c, and 5d) or even to zero, saying the transition to regular patterns or homogeneous states. This result often suggests the synchronization of dynamics between layers, especially in the cases where higher values of plankton vertical migration rates are taken, consistent with the prior migration-driven coupling mechanisms [16, 35].

Similar results can be found for the case in Figure S2, where the variation of $h_1$ and $r_2$ controls the occurrence of Hopf instability, and the $n$-patch-size patterns continue to emerge regardless of changes in $r_1$, $D_{21}$, and $h_2$. The increase of $h_1$ and $r_2$, if the values cross the threshold of Hopf–Turing instability, directly takes the system to spatially homogenous and temporally oscillating states which then transit to spatially homogenous stationary states with the disappearance of Hopf instability. The phytoplankton diffusion rate $D_{11}$ can exert an influence on the number of patch-sizes and causes the occurrence of regular patterns at very low values. Comparing the results in Figures 4–5 and S1–S2, it is hard to find a unified rule for the state transitions of system (2.2), indicating the complexity of spatiotemporal structures for the plankton patchiness, especially when the growth,

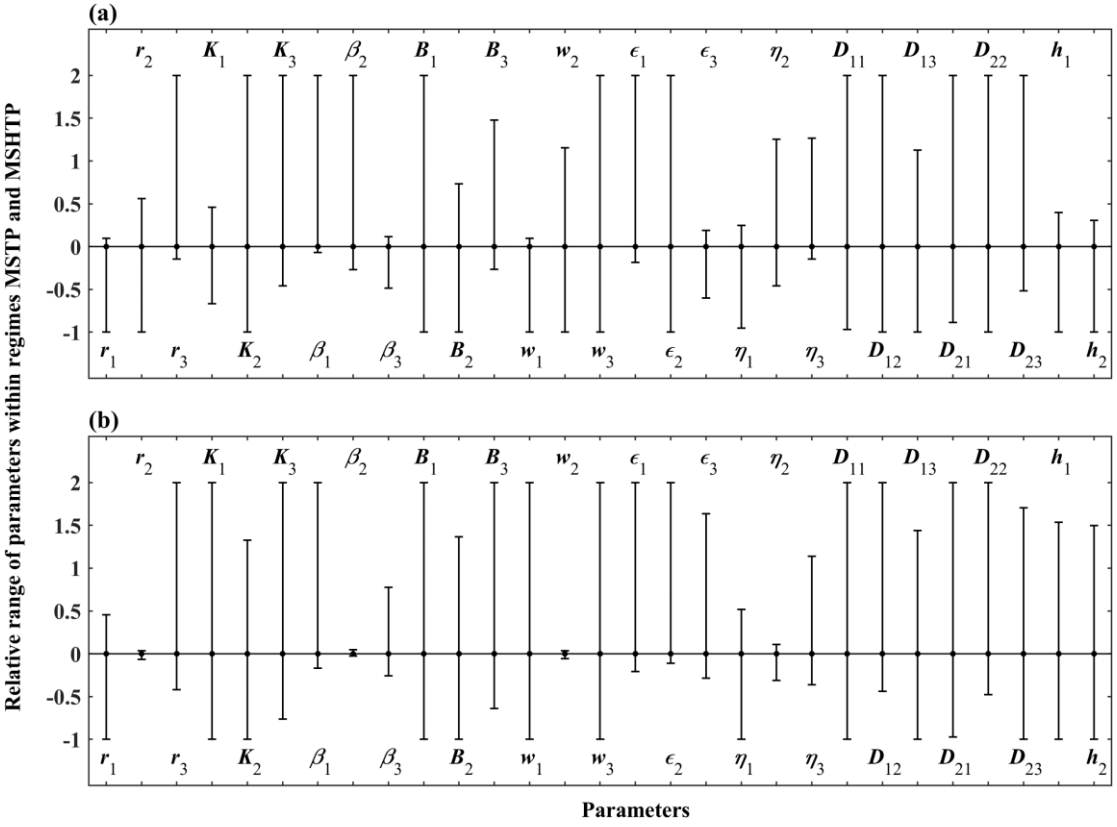


FIGURE 6. Local sensitivity ranges for the multiscale pattern regimes. Each parameter $\varphi$ is varied relative to its baseline $\varphi_0$ (all other parameters fixed), and the admissible interval of $(\varphi-\varphi_0)/\varphi_0$ for which MSTP **and** MSHTP persist is shown for (a) the pure Turing baseline used in Figure 4 and (b) the Hopf–Turing baseline used in Figure 5. Bars reaching the limits (–1 to 2) indicate no regime exit within the tested range.

predation, motility parameters are greatly influenced by the environments. Nevertheless, quantitative prediction can be performed in specific cases to understand the changes of plankton patchiness.

Figure 6 provides local sensitivity analysis of the combined multiscale regime (MSTP and MSHTP) around two baseline solutions. The bar length for each parameter reports the admissible relative interval over which multiscale structure persists when all other parameters are fixed. Therefore, short bars indicate high sensitivity (multiscale is lost after a small perturbation) and long bars indicate robustness (multiscale persists across a broad interval). Bars reaching the scan limits $(-1, 2]$ mean that no exit from the multiscale regime was detected within the tested range, implying that the multiscale condition is comparatively insensitive to that parameter over the explored interval.

For the baseline of the pure Turing instability case (Fig. 6a), sensitivity is expressed mainly through parameters that control inter-layer coupling and local reaction time scales, while horizontal diffusion is comparatively robust. In particular, the admissible ranges for the vertical exchange/migration rates $h_1$ and $h_2$ are comparatively narrow, indicating that multiscale patchiness is sensitive to how strongly the layers are coupled. Among the local reaction terms, the growth-loss balance parameters (growth $r_i$ and mortality $\eta_i$) show stronger sensitivity than "capacity/efficiency" terms, consistent with the standard mechanism that diffusion-driven pattern selection depends on the ratio of reaction time scales to transport coupling [25, 33, 34]. By contrast, the diffusion coefficients ($D_{11}$, $D_{12}$, $D_{13}$, $D_{21}$, $D_{22}$, $D_{23}$) display long admissible relative ranges (often extending far toward

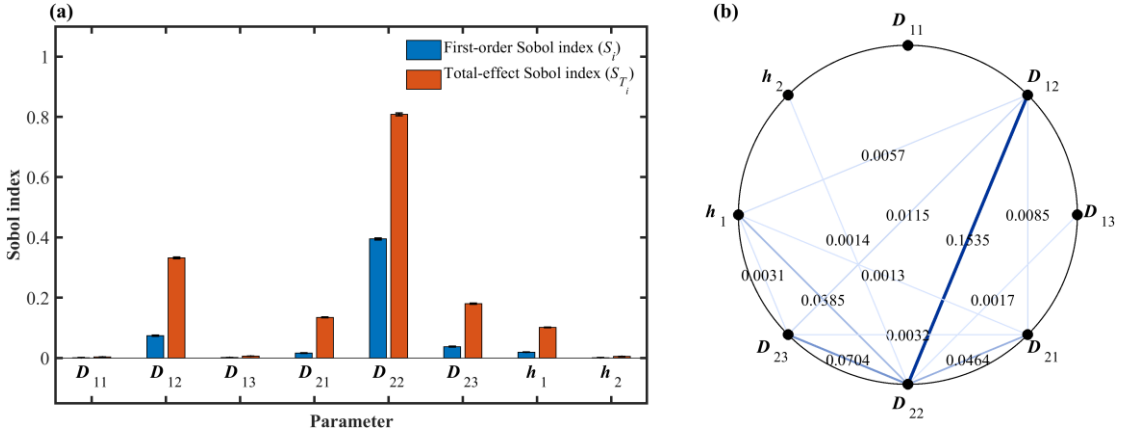


FIGURE 7. Global sensitivity of the multiscale pattern regime (MSTP and MSHTP) to mobility parameters. Sobol's indices are computed for ($D_{11}$, $D_{12}$, $D_{13}$, $D_{21}$, $D_{22}$, $D_{23}$, $h_1$, $h_2$) using a Saltelli base sample size N=1000000 and wavenumber step $m_{step}$=0.001. (a) First-order $S_i$ and total-effect $S_{Ti}$ indices with 95% bootstrap CI; (b) Significant positive pairwise interactions $S_{ij}$ (95% CI lower bound $> 0$), shown as a chord diagram with edge labels.

the scan bounds). Consequently, the diffusion parameters are not the most sensitive controls. Instead, within the tested ranges, the multiscale regime appears more limited by inter-layer coupling and reaction kinetics than by modest changes in horizontal dispersal.

For the baseline of the Hopf–Turing instability case (Fig. 6b), the strongest local sensitivities concentrate in the second layer parameters that regulate the coupled vertical-temporal dynamics required for multiscale structure. In particular, layer-2 reaction terms (most clearly, $r_2$, $\eta_2$, $\beta_2$, and $B_2$) exhibit the tightest admissible intervals, indicating that small perturbations to the second-layer production–consumption balance readily remove secondary positive dispersion peaks and collapse multiscale structure. This layer-2 sensitivity is mechanistically consistent with the three-layer coupling: the intermediate layer functions as a dynamical relay linking upper and lower layers, so changing its intrinsic reaction time scale and trophic feedback strength strongly affects whether multiple spatially unstable modes can coexist. Vertical exchange parameters remain important in this baseline because they modulate inter-layer coherence and oscillatory involvement, whereas diffusion coefficients again remain comparatively tolerant over the tested ranges, indicating that the persistence of MSTP/MSHTP is governed more by layer-2 kinetics and vertical coupling than by fine-tuning horizontal diffusion alone.

Figure 7 provides a global and variance-based ranking of which mobility parameters control the occurrence of the combined multiscale pattern regime across their full prescribed ranges. Figure 7a reports first-order Sobol indices $S_i$, which measure the standalone contribution of each parameter to the variance of the multiscale indicator $Y$, and total-effect indices $S_{Ti}$, which quantify the overall contribution including all higher-order couplings. Consequently, parameters with large $S_{Ti}$ are the dominant global controls, while large gaps $S_{Ti} - S_i$ indicate effects that are primarily expressed through interactions. The error bars (95% bootstrap CI) indicate estimation uncertainty, and hence parameters whose CIs are close to zero contribute negligibly at the explored scales.

As shown in Figure 7a, the global control is highly concentrated in a small subset of mobility parameters, with $D_{22}$ acting as the dominant driver. Specifically, $D_{22}$ shows a large $S_i$ and an even larger $S_{Ti}$, indicating that the zooplankton diffusion in layer 2 both independently determines multiscale pattern occurrence and also participates strongly in interaction effects. The next most influential parameter is $D_{12}$, whose $S_i$ is modest but $S_{Ti}$ is much larger, implying that $D_{12}$ primarily affects multiscale emergence through coupling with other mobility terms rather than acting alone. Moderate total effects are also observed for $D_{23}$ and $D_{21}$, while $h_1$ has a smaller but non-negligible contribution. In contrast, $D_{11}$, $D_{13}$, and $h_2$ remain near zero in both $S_i$

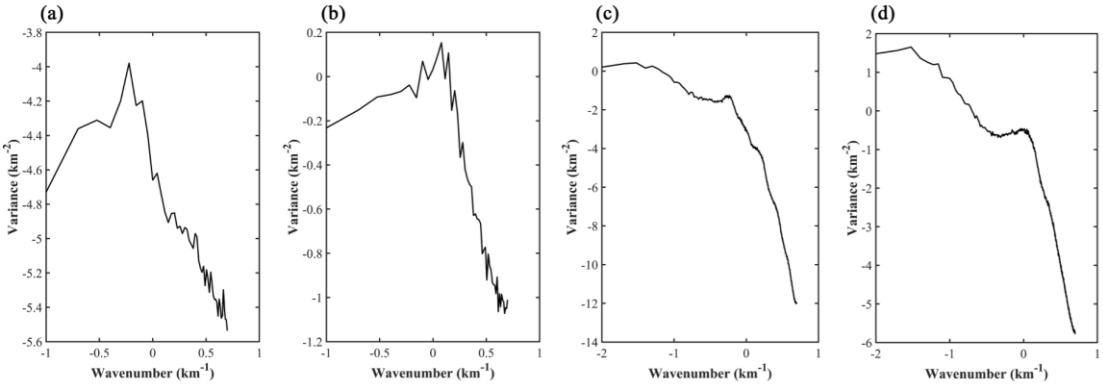


FIGURE 8. Averaged variance spectra of phytoplankton density with respect to spatial scales for the four cases of patterns in Figures 1 and 2. Panels (a)–(d) correspond to Figures 1b, 1d, 2b, and 2d, respectively.

and $S_{Ti}$, suggesting that within the tested ranges and this regime definition, multiscale pattern occurrence is comparatively insensitive to those terms. Importantly, this global ranking does not contradict the long admissible intervals seen in Figure 6 for several diffusion coefficients.

Figure 7b identifies which pairwise couplings are robustly positive drivers of multiscale pattern emergence (edges shown only when the 95% bootstrap CI lower bound for $S_{ij}$ exceeds zero), and it reveals a strongly "hub-like" interaction structure centered on $D_{22}$. The dominant interaction is $D_{12}$–$D_{22}$ with $S_{ij}\approx 0.1562$, indicating that multiscale pattern regimes are most strongly promoted when the relative horizontal mobility of phytoplankton and zooplankton in layer 2 is jointly tuned, consistent with the idea that differential dispersal between trophic levels reshapes the dispersion-relation curve geometry and enables multiple positive peaks. Secondary interactions further connect $D_{22}$ to $D_{23}$ ($\approx 0.0601$), $h_1$ ($\approx 0.0414$), and $D_{21}$ ($\approx 0.0351$), implying that multiscale pattern emergence is reinforced when layer-2 consumer dispersal co-varies with (i) consumer dispersal in another layer and (ii) vertical coupling of the phytoplankton layer. Additional weaker but significant links include $D_{22}$–$D_{11}$, $D_{12}$–$h_1$, $D_{21}$–$D_{12}$, and $D_{23}$–$h_1$. The absence of significant edges involving $h_2$ in this run indicates that zooplankton vertical exchange does not form a robust positive pairwise interaction, whereas multiscale structure is mainly governed by horizontal mobility contrasts and their coupling to $h_1$ through cross-layer feedbacks.

### 3.3. Variance spectra of plankton distribution: combined effects of heterogeneous carrying capacity and Turing instability

The plankton patterns can be analyzed by variance spectra which describe the variance of plankton density changes as a function of spatial scales. Previous research works have demonstrated that the variance spectra often follow a power-law form within a certain range of length scales [2, 6, 7, 9, 24, 33], $\mathrm{Var}(P(m)) = m^{\gamma}$, where Var and $m$ represent the variance and the wavenumber, respectively, and $\gamma$ is a negative exponent and $|\gamma|$ is the spectral slope. As a representative analysis, here we analyze the variance spectra of the phytoplankton density for the four cases of patterns in Figures 1 and 2. The results as displayed in Figure 8 describe that the patterns induced by pure Turing instability indeed show characteristics of a power-law distribution of variance spectra if the spatial scale is below 1 km. The descending spectral slopes in Figure 8a-b are calculated as $1.35\pm0.10$ and $1.97\pm0.13$, respectively.

For the patterns induced by Hopf–Turing instability, the power-law distribution of variance spectra with respect to spatial scales can be divided into two segments. When the spatial scales are above 1 km, the spectral slopes are $1.80\pm0.18$ and $1.33\pm0.12$ in Figure 8c and d. Meanwhile very steep spectra slopes are found when the spatial scales are below 1 km, even exceeding 8. The two segments of variance distribution clearly distinguish the two sizes of patches influenced by different parts of Hopf–Turing instability: the segment of larger spatial scales

is affected by $\max(\lambda_s(0))$, whereas the other segment is dominated by the right peaks (which are corresponding to smaller patch sizes) on the dispersion relation. In comparison with the results in literature [2, 6, 7, 9, 24, 33], it suggests that the pure Turing instability exerts primary effects on the emergence of the patches below 1 km. On the spatial scales over 1 km, the Hopf–Turing instability can shape the distribution of plankton density.

In order to make the patterns closer to previous predictions and field observations, we further introduce environmental heterogeneity to the dynamics of system (2.2). Referring to the work of Abraham [7], we set spatially heterogeneous distribution for the carrying capacity $K$: the carrying capacity continually relaxes towards a zonally varying background value, $K^*_{i0} = K_{i0}\ (1 + \theta\cos(2\pi x/L_x)/2)$, and the dynamic change of carrying capacity is described as $\mathrm{d}K/\mathrm{d}t = \alpha(K^*_{i0} - K)$. The relaxation rate is set at $\alpha = 0.25$, the parameter $\theta$ is given as 0.01, 0.1, and 1 to represent three degrees of carrying capacity heterogeneity, and the domain size along $x$-direction, $L_x$, is taken as 256 km. The spatial step for plankton pattern formation is still set as 1 hm. Here, we perform the simulations of pattern formation corresponding to the cases of Figure 1b and Figure 2d, and the pattern results and variance spectrum analysis are plotted in Figures 9–10, respectively. For comparison with previous works [2, 7, 9, 33], linear regression of spectra slopes is carried out at the spatial scales larger than 5 km. This is adequate since this scale range is also in coincidence with the segment of larger spatial scales on the spectra curves.

Figure 9a–c demonstrates that the emergence of nested patterns on the background of heterogeneous carrying capacity. Interestingly, the conditions for pure Turing instability restrict where the patterns can occur with the variation of $K$ in the space. When the heterogeneity of carrying capacity is weak ($\theta = 0.01$), the distribution of plankton density maintains the similar nested structure as described in Figure 1b in every local area and the variation is very low globally (Fig. 9a). With the increase of $\theta$, the local variation of plankton distribution is far smaller than the global variation induced by environmental heterogeneity (Fig. 9b), and even in the areas with low $K$ values homogeneous states occur (Fig. 9c). Reflected in the variance spectra, that is the rapid rise of the spectra slope with the increase of the carrying capacity heterogeneity, as shown in Figure 9d–f.

Figure 10 shows the patterns self-organized under the combined effect of Hopf–Turing instability and carrying capacity heterogeneity. Likewise with the increase of heterogeneous carrying capacity as underlying background, the plankton-free areas gradually expand. Moreover, although the patches with nested structure still take place, these patches converge tightly to form parallel bands perpendicular to the $x$-direction (Fig. 10a–c). Since the Hopf–Turing instability has the ability to influence plankton distribution at the spatial scales where carrying capacity heterogeneity generates, the effects of Hopf–Turing instability and carrying capacity heterogeneity on the pattern formation are neutralized with each other. Reflected in the variance spectra (Fig. 10d–f), the spectra slope is even reduced under the influence of heterogeneous carrying capacity with $\theta = 0.01$, if we compared it with that in Figure 8d. Spectra slope reaches the highest as 2.02±0.23 with the intermediate degree of carrying capacity heterogeneity and then drops to 1.59±0.31 with the increase of heterogeneity degree. This result suggests that moderate rather than maximal environmental heterogeneity can lead to significant distributional differences of plankton density.

The spectra slopes observed or predicted in previous studies show values of 0.65±0.25 [2], 2.10±0.20 [7], 5/3 and 2 [9, 33]. A comparison suggests that the Hopf–Turing instability can yield reasonable predictions for the characteristics of plankton patchiness. Another interesting question is what role pure Turing instability plays in such patchiness characteristic. Hence, we combine the patterns induced by pure Turing and Hopf–Turing instability, denoted as $P_{i-PT}$ and $P_{i-HT}$, and then analyze the variance spectra. Assume the ecosystem has $M$ pairs of phytoplankton-zooplankton interaction and we study the combination $(M\text{-}1)P_{i-PT}+P_{i-HT}$. Using Figure 9c and 10c as example, $M = 2$ and 3 lead to spectra slopes 1.89±0.30 and 2.13±0.25, respectively (Fig. S3). The result is very close to that given in previous research [7, 9, 33]. Moreover, the increase of $M$ keeps the result in a reasonable range, such as 2.47±0.23 for $M = 6$ and 2.76±0.25 for $M = 11$ (Fig. S3). This suggests the result for the combined patterns is not a coincidence. The combination of Hopf–Turing and pure Turing instability under environmental heterogeneity is also a possible way for predicting plankton patterns occurring in natural ecosystems.

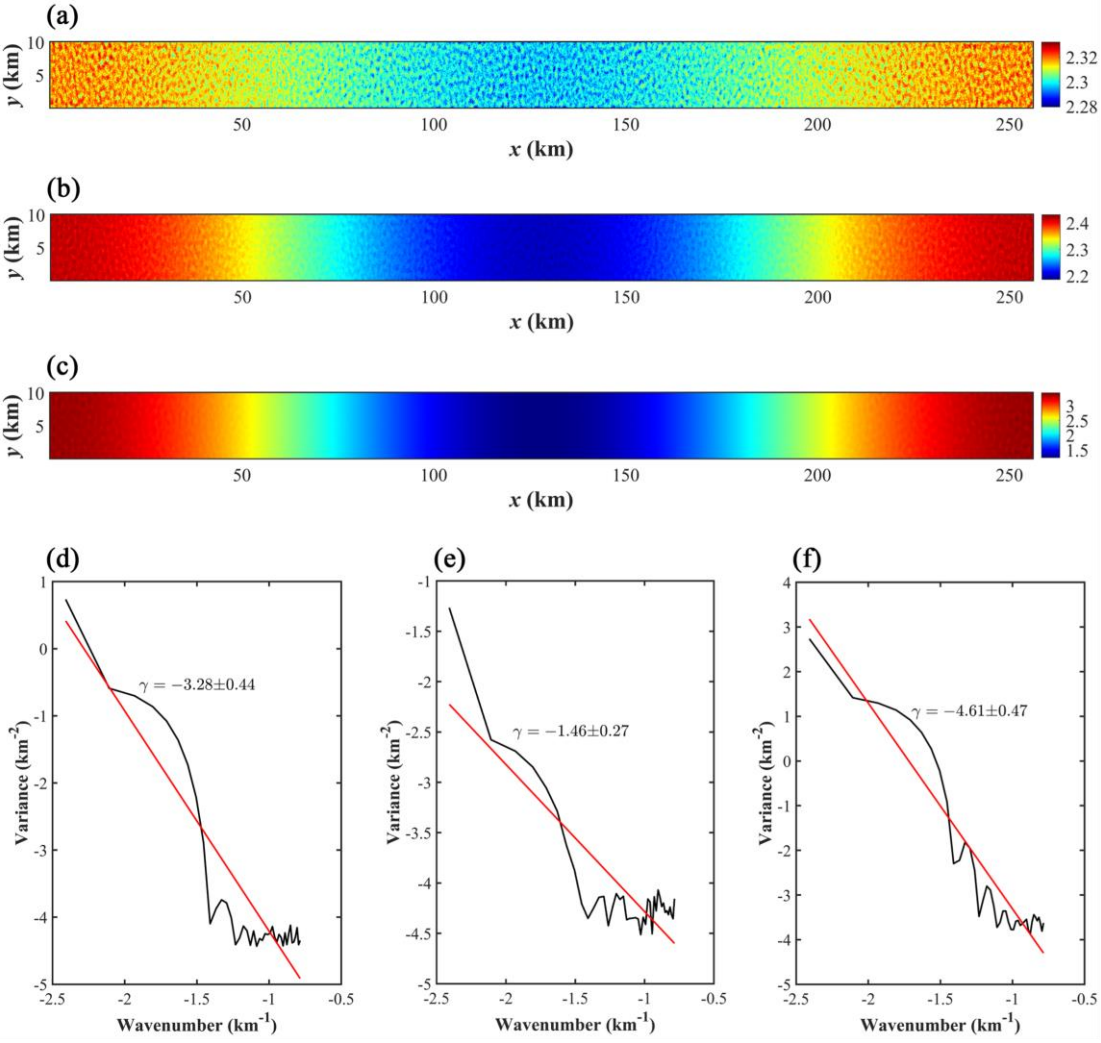


FIGURE 9. Self-organization of phytoplankton patterns under pure Turing instability when the carrying capacity is heterogeneous with (a) $\theta = 0.01$, (b) $\theta = 0.1$, (c) $\theta = 1$, and (d–f) the averaged variance spectra corresponding to (a)-(c), respectively. The parametric conditions are the same as those in Figure 1b.

## 4. Discussion and extensions

The mechanisms for the emergence of plankton patchiness have been a research focus in recent decades. Previous studies have highlighted that patchiness can arise from both ecological interactions and physical forcing, and that their interplay often produces variability across a wide range of spatial scales. In this research, with the consideration of plankton vertical migration, a spatiotemporal phytoplankton-zooplankton model coupled with three reaction–diffusion subsystems is established. By representing a vertically water column as three horizontally extended layers linked by migration, the model provides a minimal framework to examine how vertical environmental heterogeneity reshapes horizontal self-organization. The exploration on the coupled system discovers new types of Turing instability that lead to the emergence of complex patterns with the co-occurrence of different sizes of patches. The discovery extends previous research [29, 30] on the nested structures of the

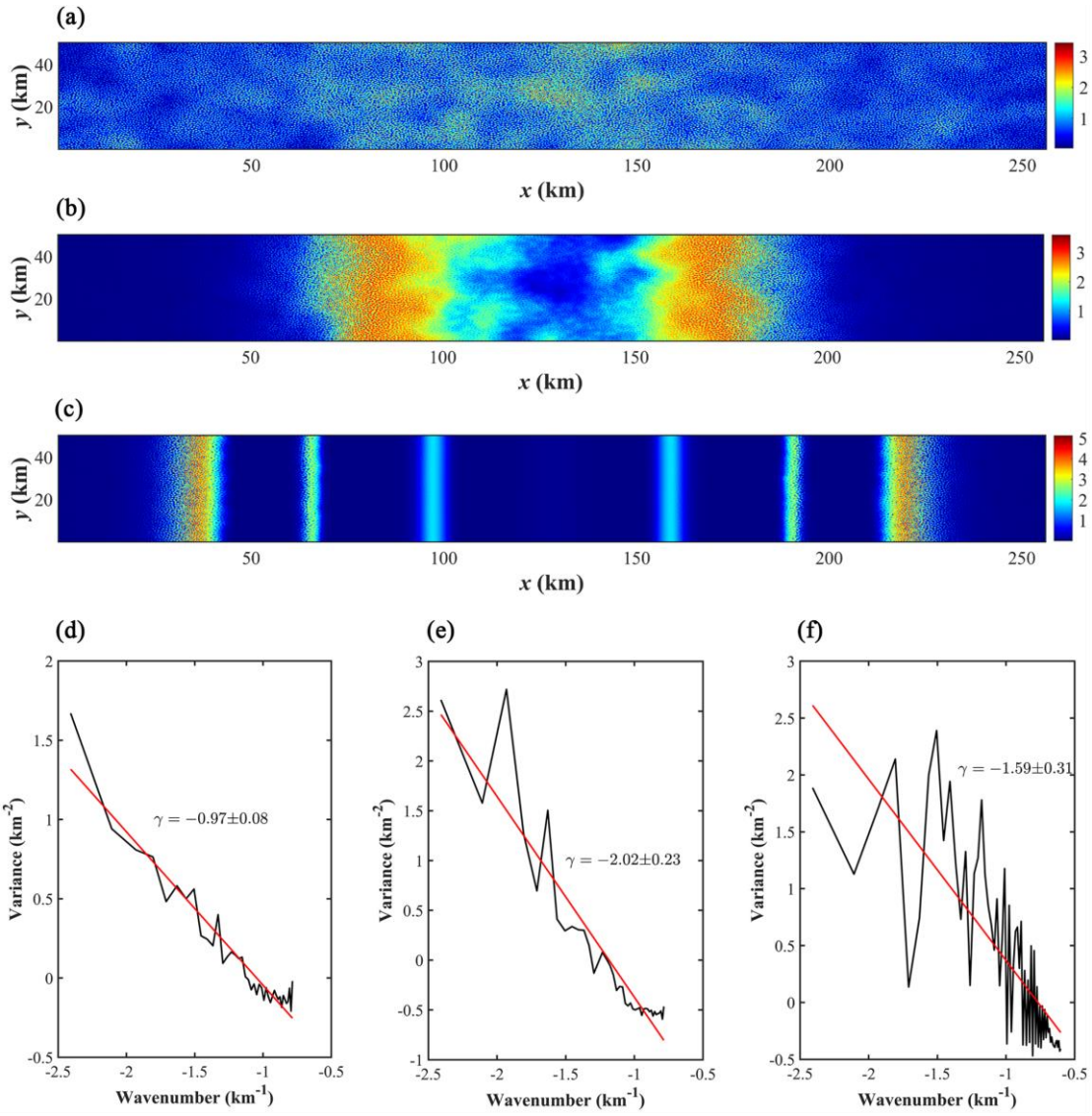


FIGURE 10. Self-organization of phytoplankton patterns under Hopf–Turing instability when the carrying capacity is heterogeneous with (a) $\theta = 0.01$, (b) $\theta = 0.1$, (c) $\theta = 1$, and (d–f) the averaged variance spectra corresponding to (a)–(c), respectively. The parametric conditions are the same as those in Figure 2d.

plankton patterns: firstly, the patterns with three-size patches are found; secondly, the patches of different sizes can co-occur in parallel or nested way; thirdly, Hopf–Turing instability induces nested structures that exist between irregular and regular patches. These new results suggest that the Turing instability can successfully interpret the self-organization of complex patterns where plankton patches of multiple sizes and various shapes interweave with each other. Plankton vertical migration not only connects but also synthesizes the dynamics between different water layers, allowing pattern features to be transferred and combined across depth and thereby generating new spatiotemporal structures.

The emergence of the $n$-patch-size patterns with subtle structures is related to the peaks on the dispersion relation. When pure Turing instability takes place, a typical instance is the nested patterns with smaller patches embedded into larger ones, which are corresponding to the dispersion relation with two peaks. This instance has already been studied in detail by previous approach [30]. The improvement in this research is that we further demonstrate the corresponding relation between the three-patch-size patterns and the dispersion relation with three peaks. Moreover, the sizes of the patches can be calculated by the wavenumbers determined by the peaks. When Hopf–Turing instability occurs, the existence of more than one peak on the dispersion relation remains a key condition for the emergence of nested patterns, because distinct unstable modes can simultaneously imprint spatial organization at separated scales. The two sizes of plankton patches in the patterns have very large difference, suggesting that the Hopf–Turing instability in this case can simultaneously shape the spatial distribution of plankton at two different scales. It is demonstrated previously that the irregular or spiral wave patches induced by Hopf–Turing instability have chaotic characteristics [29, 31], and therefore this case of nested pattern holds a structure of larger wandering irregular patches carrying smaller regular patches, briefly, "chaotic carrying regular" structure. More generally, the "peak-count → patch-size-count" correspondence offers a practical diagnostic: it links linear stability fingerprints (number and separation of peaks) to nonlinear outcomes (parallel versus nested co-occurrence) and helps interpret why additional layers and migration can unlock richer multi-scale structures than single-layer systems.

The variance in the distribution of plankton patchiness in natural ecosystems often follows the power-law form with the variance of spatial scales. In this research, the variance spectrum analysis on the discovered patterns leads to similar results. In comparison with previous works, we find that using 1 km as the dividing scale, the pure Turing instability mainly affects the plankton distribution at smaller scales, whereas the Hopf–Turing instability exerts influence at larger scales. Calculating the spectra slopes for the patterns demonstrates that the two instability mechanisms can lead to reasonable slope ranges ($1\sim2$) in their corresponding dominant scales. On the basis of Turing instability mechanism, heterogeneous carrying capacity is further introduced. The effects of carrying capacity heterogeneity and Hopf–Turing instability can be neutralized and their combined effects still make proper prediction for the plankton distribution at the spatial scales over 5 km. Moreover, with the consideration of carrying capacity heterogeneity, it is found that the combination of Hopf–Turing and pure Turing instability can also provide possible explanation for the emergence of plankton patchiness characteristic occurring in natural ecosystems. These results emphasize that variance spectra provide a compact, scale-resolved summary of pattern outcomes: multi-patch-size organization typically broadens the range of active scales and tends to yield power-law-like spectra over larger scale bands, whereas single dominant patch size often produces steeper or more localized spectral signatures.

Environmental heterogeneity can be reflected in the variation of other parameters at different spatial scales, like the heterogeneous carrying capacity considered in this research. The key point is that the Turing instability influences the plankton patches at the scales where environmental heterogeneity occurs. Thus, the distribution of plankton density can be shaped by the combined effects of the two factors. For the coupled phytoplankton-zooplankton system, the variations of parameters can lead to very complex transitions of system states. The distribution of state areas along the increase of system parameters may show discrete characteristic, *i.e.*, the system state can suddenly jump between $n$-patch-size ($n > 2$) patterns, homogeneous states, and regular patterns. Varying different parameters can lead to distinct state transitions and corresponding change of plankton patch-sizes. Therefore, it suggests when the environmental heterogeneity enhances spatially to affect more parameter values, richer patch-sizes of plankton distribution may be present across the spatial scales. This is important since the number of plankton patch-sizes has a crucial effect on the variance spectra slope, which is an inference that can be deduced from the variance spectrum analysis for the patterns. For instance, comparing the spectra slopes of patterns induced by pure Turing and Hopf–Turing instability at scales below 1 km (Fig. 8), single patch size leads to steep slopes at this scale, whereas $n$-size ($n > 2$) patches push the spectra slopes to a reasonable range. Hence, environmental heterogeneity crossing multiscales should be also responsible to explain the plankton patchiness in natural ecosystems since $n$-size patches can be created with its involvement. In this context, two ecologically important sources of heterogeneity that are not explicitly represented in this study are (i) nutrient limitation, which introduces resource-biomass feedbacks and additional timescales, and

(ii) turbulent stirring, which continuously deforms spatial structures and transfers variance across scales. To examine whether the multiscale patchiness persists under these more realistic ingredients, we here considered two minimal extensions and analyzed their pattern outcomes and spectra (Figs. 11, 12 and S4).

A natural ecological generalization of equation (2.2) is to introduce an explicit nutrient field that limits phytoplankton growth and is depleted by uptake. For each layer $i = 1, 2, 3$, a minimal nutrient-phytoplankton-zooplankton form can be written as

$$\frac{\partial R_i}{\partial t} = I_i - u_i P_i \frac{R_i}{C_i + R_i} - \upsilon_i R_i + h_R \left( \sum_{j \in \Omega_i} R_j - N_i R_i \right) + D_{Ri} \nabla^2 R_i, \tag{4.1a}$$

$$\frac{\partial P_i}{\partial t} = r_i P_i \frac{R_i}{C_i + R_i} \left( 1 - \frac{P_i}{K_i} \right) - \frac{\beta_i P_i Z_i}{B_i + P_i + w_i Z_i} + h_1 \left( \sum_{j \in \Omega_i} P_j - N_i P_i \right) + D_{1i} \nabla^2 P_i, \tag{4.1b}$$

$$\frac{\partial Z_i}{\partial t} = \frac{\varepsilon_i \beta_i P_i Z_i}{B_i + P_i + w_i Z_i} - \eta_i Z_i + h_2 \left( \sum_{j \in \Omega_i} Z_j - N_i Z_i \right) + D_{2i} \nabla^2 Z_i. \tag{4.1c}$$

where $R_i$ is the nutrient concentration, $C_i$ is the half-saturation constant, $I_i$ is the external nutrient supply, $u_i$ is the maximum uptake rate, and $\upsilon_i$ is the nutrient loss/decay rate, with $h_R$ and $D_{Ri}$ describing inter-layer exchange and horizontal diffusion of nutrients, respectively. Figure 11 shows that introducing nutrient limitation does not eliminate multiscale patchiness. Instead, it reshapes pattern contrast by adding a stabilizing resource feedback and by allowing resource gradients to modulate where phytoplankton patches can persist. Like the patterns shown in Figures 1d and 2d, Figures 11a–c and 11d–f also exhibit the emergence of multiscale patchiness induced by pure Turing and Hopf-Turing instabilities. Ecologically, this indicates that multi-patch-size structures need not rely on "fixed" habitat heterogeneity. They can also be sustained under internally generated heterogeneity arising from nutrient-biomass interactions.

Oceanic plankton fields are continuously stretched and folded by horizontal stirring, which can both create filamentary patchiness and redistribute variance across scales. To represent this effect while retaining the ecological mechanisms in equation (2.2), we coupled the three-layer system to a seeded-eddy turbulent flow as modeled by Abraham [7] and applied identically to all layers. The parametric conditions for the turbulent flow model are the same as those in the literature [7] except that the space step is taken as 1 hm for simulating the population dynamics. Numerically, each time step is split into (i) an advection/stirring step that moves grid parcels according to the turbulent velocity field and (ii) a biological step that applies reaction, diffusion, and vertical migration on the updated neighborhood topology. Figure 12 demonstrates that turbulent stirring strongly deforms biologically generated patches, producing elongated filaments and intermittent high-contrast structures, while reaction–diffusion-migration continuously regenerates biomass gradients and maintains persistent patchiness (Fig. 12a, b). Because the horizontal flow is imposed on all layers, coherent large-scale features can be shared across depth. At the same time, layer-specific parameters and vertical migration can produce distinct amplitudes and fine-scale differences among $P_i$ and $Z_i$. Figure S4 repeats the turbulence-coupled simulations on a different domain size, showing that changing the domain can preserve the qualitative coexistence of biologically selected patch sizes and turbulence-induced deformation.

To place the model spectra in an observational context, we analyzed satellite-derived surface chlorophyll-$a$ in the Bohai and Yellow Seas (Fig. 13) using the same variance-spectrum procedure applied to model outputs. Figure 13 shows that the BYS chlorophyll fields exhibit clear scale dependence and can be approximated by power-law variance spectra over 4–800 km, with seasonally varying slopes (reported as mean ± standard deviation across transects). This empirical benchmark is consistent with the central implication of our modeling results: multiscale plankton patchiness can produce approximately power-law spectra over broad scale bands, and the spectral exponent is sensitive to the relative importance of mechanisms acting at different scales.

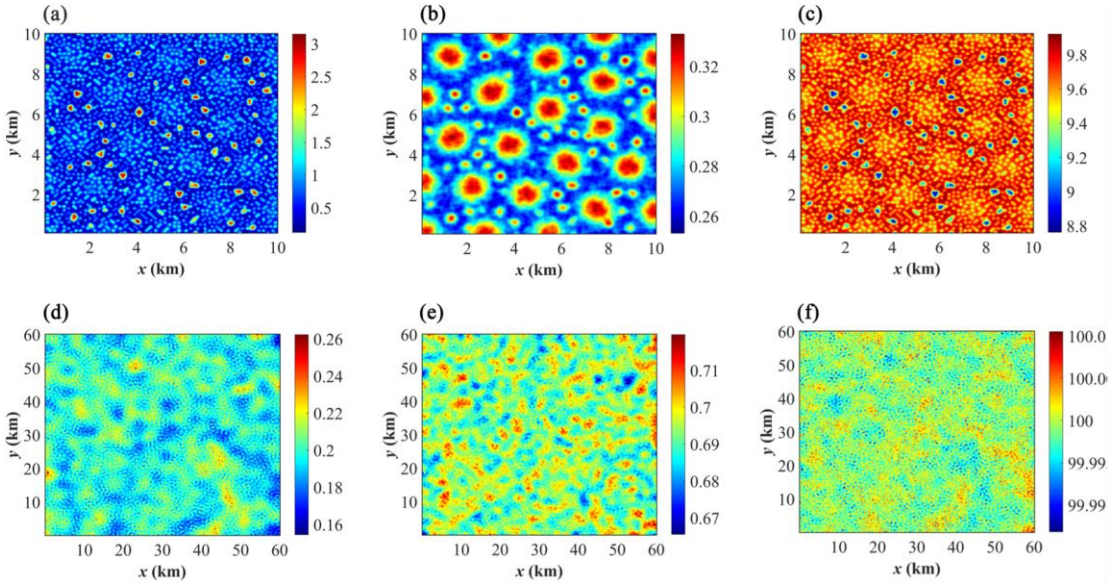


FIGURE 11. Multiscale pattern formation in the three-layer nutrient-phytoplankton-zooplankton extension as described in Eq. (4.1). The resulting spatial distributions illustrate that multiscale patchiness can persist when an explicit nutrient variable is included. The nutrient-related parameter values are given in Table S2, and the other parametric conditions for (a–c) and (d–f) are the same as Figures 1d and 2d, respectively.

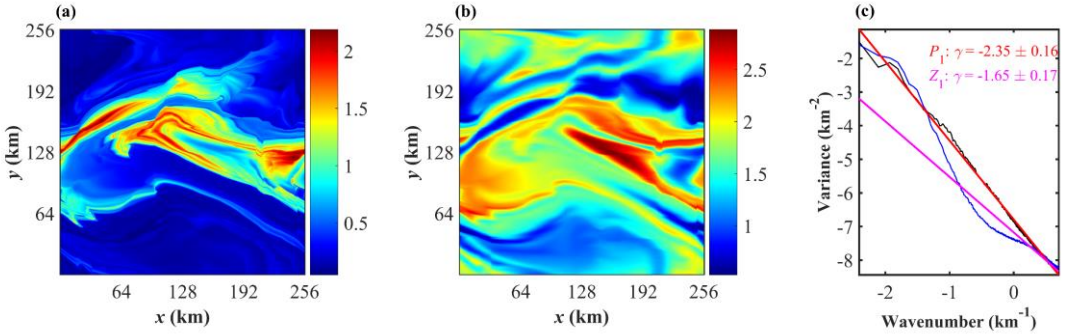


FIGURE 12. Turbulence-coupled plankton patchiness on a $L = 256$ km periodic domain. The three-layer phytoplankton-zooplankton dynamics is coupled to a turbulent flow using a seeded-eddy turbulent flow model. The turbulent flow parametric conditions are the same as those in the literature [7] and the parametric conditions for plankton dynamics are the same as Figure 2d. Panels (a) and (b) show the representative spatial distributions of $P_1$ and $Z_1$ after truncating transients, and panel (c) is the averaged variance spectra of the two plankton patterns with respect to spatial scales.

The modeled variance-spectrum characteristics are comparable to those observed in surface chlorophyll-$a$ fields from the Bohai and Yellow Seas. The turbulence-coupled simulations yield power-law exponents as $\gamma_{P1} \approx -2.35$ (Fig. 12c) and $\gamma_{P1} \approx -1.67$ (Fig. S4c), respectively, over the fitted patch-scale band. These turbulence-coupled slopes are comparable to the large-scale Hopf–Turing segment reported in Section 3.3 for the system (2.2) without explicit stirring (*e.g.*, $\gamma \approx -1.33$ to $-1.80$ for the kilometer-above segment in

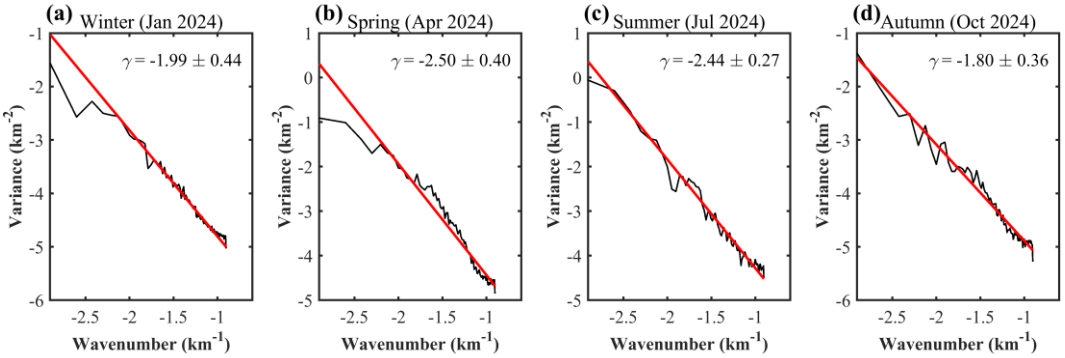


FIGURE 13. Averaged variance spectra of surface chlorophyll-$a$ in the Bohai and Yellow Seas across seasons. For each season, variance spectra are computed along multiple 800 km transects, averaged across transects, and regressed in log–log space to estimate the power-law exponent $\gamma$.

Figure 8c, d), and overlap with the "heterogeneous carrying capacity" cases where environmental forcing projects variance onto larger scales (*e.g.*, $\gamma \approx -1.59$ to $-2.02$ for the >5 km fits in Figure 10d–f). The chlorophyll spectra of Bohai and Yellow Seas in Figure 13 fall within a similar band, with seasonal means $\gamma = -1.99 \pm 0.44$ (winter, Fig. 13a), $-2.50 \pm 0.40$ (spring, Fig. 13b), $-2.44 \pm 0.27$ (summer, Fig. 13c), and $-1.80 \pm 0.36$ (autumn, Fig. 13d) over 4–800 km. Overall, these exponents are consistent with commonly reported oceanic ranges (*e.g.*, $\gamma \approx -0.65 \pm 0.25$, $\gamma \approx -2.10 \pm 0.20$, and theoretical scaling $\gamma \approx -5/3$ to $-2$) [2, 7, 9, 33]. Such theoretical and observational consistency supports a unified picture where intrinsic instabilities and vertical exchange select preferred biological patch sizes, whereas heterogeneity and horizontal stirring redistribute variance and can extend the effective scaling range observed in spectra.

The improvement of this research is reflected in two aspects. Compared with previous works that explain the emergence of plankton patchiness through Turing instability [25–27, 31, 33], we discover the new mechanisms of Turing instability for the emergence of complex patterns with two or three sizes of plankton patches. A few approaches have also predicted the variance spectra characteristic of plankton patchiness from the viewpoint of biophysical mechanisms [7, 9, 24]. Although the effects of turbulence flow, eddies, *etc.*, have been emphasized, however, the impact of ecological mechanisms such as self-diffusion and vertical migration of plankton has received insufficient discussion. In this research, we demonstrate that the Turing instability with more than one peak on the dispersion relation can cause the self-organization of patterns that have properties close to the those observed records. On the basis of this approach, we can further explicitly include complex physical processes in the model and explore how the Turing instability mechanism interacts with physical mechanisms for generating complex plankton patterns in future studies.

## 5. CONCLUSIONS

This study developed a three-layer coupled phytoplankton-zooplankton reaction–diffusion model that incorporates vertical exchange/migration of plankton. Linear stability analysis and numerical simulations showed that the coupled system can generate multiscale plankton patchiness through both pure Turing and Hopf–Turing instabilities. A key result is that multi-peak dispersion relations provide a mechanistic signature of patterns with two or three coexisting patch sizes, including both parallel and nested spatial organizations.

The results reveal a clear scale-dependent role of the two instability mechanisms. Pure Turing instability mainly shapes plankton patchiness below about 1 km, whereas Hopf–Turing instability has a stronger influence on larger-scale structures. Parameter sweeps and sensitivity analyses indicate that multiscale pattern regimes are governed primarily by inter-layer coupling and a small subset of mobility parameters, especially the transport properties of the intermediate layer. When spatially heterogeneous carrying capacity is introduced, the model yields variance-spectrum slopes consistent with those reported in previous studies.

By further considering nutrient limitation, turbulence, and comparison with satellite-derived chlorophyll-*a* spectra from the Bohai and Yellow Seas, this work demonstrates the robustness and ecological relevance of the proposed mechanism. The main innovation of the study lies in unifying vertical migration and multi-peak reaction–diffusion instability within one framework, thereby providing a plausible explanation for the self-organization of multiscale plankton patchiness in natural aquatic ecosystems.

## Funding

This work is supported by the National Natural Science Foundation of China (No. 11802093) and the Fundamental Research Funds for the Central Universities (No. 2025MS078).

## Data availability statement

The dataset "Bohai and Yellow Sea surface chlorophyll-*a* concentration satellite remote sensing dataset" used in this study (Fig. 13) was obtained through an application and review process at the National Natural Science Foundation of China Qingdao Marine Science Data Sharing Service Center. Researchers may request access to this dataset by submitting a formal application through the center's data request system. For the numerical simulations and analysis, readers may contact the corresponding author to obtain the codes

## References

[1] E. Trudnowska, M. Gluchowska, A. Beszczynska-Moller, K. Blachowiak-Samolyk and S. Kwasniewski, Plankton patchiness in the polar front region of the west Spitsbergen shelf. *Mar. Ecol. Progr. Ser.* **560** (2016) 1–18.

[2] S. van Gennip, A.P. Martin, M.A. Srokosz, J. Allen, R. Pidcock, S.C. Painter and M.C. Stinchcombe, Plankton patchiness investigated using simultaneous nitrate and chlorophyll observations. *J. Geophys. Res.: Oceans* **121** (2016) 4149–4156.

[3] S.S. Urmy and J.D. Warren, Seasonal changes in the biomass, distribution, and patchiness of zooplankton and fish in four lakes in the Sierra Nevada, California. *Freshwater Biol.* **64** (2019) 1–18.

[4] M. Scheinin and E. Asmala, Ubiquitous patchiness in chlorophyll a concentration in coastal archipelago of Baltic Sea. *Front. Mar. Sci.* **7** (2020) 1–12.

[5] K.L. Robinson, S. Sponaugle, J.Y. Luo, M.R. Gleiber and R.K. Cowen, Big or small, patchy all: resolution of marine plankton patch structure at micro- to submesoscales for 36 taxa. *Sci. Adv.* **7** (2021) eabk2904.

[6] M. Lévy, P.J.S. Franks and K.S. Smith, The role of submesoscale currents in structuring marine ecosystems. *Nat. Commun.* **9** (2018) 4758.

[7] E.R. Abraham, The generation of plankton patchiness by turbulent stirring. *Nature* **391** (1998) 577–580.

[8] R.E. Breier, C.C. Lalescu, D. Waas and M. Mazza, Emergence of phytoplankton patchiness at small scales in mild turbulence. *PNAS* **115** (2018) 12112–12117.

[9] K.L. Daly and W.O. Smith, Jr., Physical–biological interactions influencing marine plankton production. *Annu. Rev. Ecol. Syst.* **24** (1993) 555–585.

[10] J.C. Prairie, K.R. Sutherland, K.J. Nickols and A.M. Kaltenberg, Biophysical interactions in the plankton: a cross-scale review. *Limnol. Oceanogr. Fluids Environ.* **2** (2012) 121–145.

[11] D.J. McGillicuddy and P.J.S. Franks, Models of plankton patchiness, in: *Encyclopedia of Ocean Sciences*, edited by J.K. Cochran, H.J. Bokuniewicz and P.L. Yager, 3rd edn., Vol. 5. Elsevier, Oxford (2019) 536–546.

[12] C.L. Folt and C.W. Burns, Biological drivers of zooplankton patchiness. *Trends Ecol. Evol.* **14** (1999) 300–305.

[13] M. Bengfort, U. Feudel, E.M. Hilker and H. Malchow, Plankton blooms and patchiness generated by heterogeneous physical environments. *Ecol. Complex.* **20** (2014) 185–194.

[14] W.M. Durham, E. Climent, M. Barry, F. De Lillo, G. Boffetta, M. Cencini and R. Stocker, Turbulence drives microscale patches of motile phytoplankton. *Nat. Commun.* **4** (2013) 2148.

[15] E.A. Blukacz, W.G. Sprules, B.J. Shuter and J.P. Richards, Evaluating the effect of wind-driven patchiness on trophic interactions between zooplankton and phytoplankton. *Limnol. Oceanogr.* **55** (2010) 1590–1600.

[16] B. Chen, E. Masunaga, S.L. Smith and H. Yamazaki, Diel vertical migration promotes zooplankton horizontal patchiness. *J. Oceanogr.* **77** (2020) 123–135.

[17] A.T. Greer, C.B. Woodson, C.E. Smith, C.M. Guigand and R.K. Cowen, Examining mesozooplankton patch structure and its implications for trophic interactions in the northern Gulf of Mexico. *J. Plankton Res.* **38** (2016) 1115–1134.

[18] I. Hillmer, P. van Reenen, J. Imberger and T. Zohary, Phytoplankton patchiness and their role in the modelled productivity of a large, seasonally stratified lake. *Ecol. Model.* **218** (2008) 49–59.

[19] A.G. Degermendzhy, E.S. Zadereev, D.Yu. Rogozin, I.G. Prokopkin, Y.V. Barkhatov, A.P. Tolomeev, E.B. Khromechek, J.H. Janse, W. M. Mooij and R.D. Gulati, Vertical stratification of physical, chemical and biological components in two saline lakes Shira and Shunet (South Siberia, Russia). *Aquat. Ecol.* **44** (2010) 619–632.

[20] C. Schmoker and S. Hernández-León, Stratification effects on the plankton of the subtropical Canary Current. *Progr. Oceanogr.* **119** (2013) 24–31.

[21] F. Ríos, R. Kilian and E. Mutschke, Chlorophyll-*a* thin layers in the Magellan fjord system: the role of the water column stratification. *Continent. Shelf Res.* **124** (2016) 1–12.

[22] B. Yang, M.G. Wells, J. Li and J. Young, Mixing, stratification, and plankton under lake-ice during winter in a large lake: implications for spring dissolved oxygen levels. *Limnol. Oceanogr.* **65** (2020) 2713–2719.

[23] V. Venkataramana, R.K. Mishra, P. Sabu, N. Anikumar, A. Sarkar, R.K. Naik, M.A. Soares and L. Gawade, Stratification governs the plankton community structure and trophic interaction in the Southwestern tropical Indian Ocean during boreal summer. *Reg. Stud. Mar. Sci.* **48** (2021) 101987.

[24] W.J. McKiver and Z. Neufeld, Resonant plankton patchiness induced by large-scale turbulent flow. *Phys. Rev. E* **83** (2011) 016303.

[25] S.A. Levin and L.A. Segel, Hypothesis for origin of planktonic patchiness. *Nature* **259** (1976) 659–659.

[26] H. Malchow, B. Radtke, M. Kallache, A.B. Medvinsky, D.A. Tikhonov and S.V. Petrovskii, Spatio-temporal pattern formation in coupled models of plankton dynamics and fish school motion. *Nonlinear Anal. Real World Appl.* **1** (2000) 53–67.

[27] A.B. Medvinsky, S.V. Petrovskii, I.A. Tikhonova, H. Malchow and B.L. Li, Spatiotemporal complexity of plankton and fish dynamics. *SIAM Rev.* **44** (2002) 311–370.

[28] Q.X. Liu, Z. Jin and B.L. Li, Resonance and frequency-locking phenomena in spatially extended phytoplankton–zooplankton system with additive noise and periodic forces. *J. Stat. Mech. Theory Exp.* **2008** (2008) P05011.

[29] T. Huang, C. Yu, K. Zhang, X. Liu, J. Zhen and L. Wang, Complex pattern dynamics and synchronization in a coupled spatiotemporal plankton system with zooplankton vertical migration. *Chaos Solitons Fractals* **175** (2023) 114063.

[30] T. Huang, C. Yu, Z. Lin, H. Zhang, R. Liu, R. Li, Y. Yang and Y. Tian, Self-organization of nested patterns in a coupled spatiotemporal phytoplankton–zooplankton system. *Commun. Nonlinear Sci. Numer. Simul.* **130** (2024) 107804.

[31] W. Wang, S. Liu and Z. Liu, Spatiotemporal dynamics near the Turing–Hopf bifurcation in a toxic–phytoplankton–zooplankton model with cross-diffusion. *Nonlinear Dyn.* **98** (2019) 27–37.

[32] G.M. Cohen and J.B. Shurin, Scale-dependence and mechanisms of dispersal in freshwater zooplankton. *Oikos* **103** (2003) 603–617.

[33] J.H. Steele and E.W. Henderson, A simple model for plankton patchiness. *J. Plankton Res.* **14** (1992) 1397–1403.

[34] S.J. Brentnall, K.J. Richards, J. Brindley and E. Murphy, Plankton patchiness and its effect on larger-scale productivity. *J. Plankton Res.* **25** (2003) 121–140.

[35] K. Bandara, Ø. Varpe, L. Wijewardene, V. Tverberg and K. Eiane, Two hundred years of zooplankton vertical migration research. *Biol. Rev.* **96** (2021) 1547–1589.

[36] L. Matthews and J. Brindley, Patchiness in plankton populations. *Dyn. Stabil. Syst.* **12** (1997) 39–59.

[37] J.M.G. Vilar, R.V. Solé and J.M. Rubi, On the origin of plankton patchiness. *Physica A* **317** (2003) 239–246.

[38] L.N. Hudson and D.C. Reuman, A cure for the plague of parameters: constraining models of complex population dynamics with allometries. *Proc. Roy. Soc. B* **280** (2013) 20131901.

[39] W. Tian, H. Zhang, Z. Wang, Y. Tian and T. Huang, Analysis on the stability of plankton in a food web with empirical organism body mass distribution. *Environ. Sci. Pollut. Res.* **30** (2022) 21327–21343.

[40] N.K. Thakur, A. Ojha and S.K. Tiwari, The role of adaptation in plankton system with Beddington–DeAngelis type functional response, in *Mathematical Modelling and Scientific Computing with Applications: ICMMSC 2018, Indore, India, July 19–21*, edited by S. Manna, B. Datta and S. Ahmad. Springer Proceedings in Mathematics & Statistics, Vol. 308. Springer, Singapore (2020) 21–33.

[41] X.C. Zhang, G.Q. Sun and Z. Jin, Spatial dynamics in a predator–prey model with Beddington–DeAngelis functional response. *Phys. Rev. E* **85** (2012) 021924.
[42] L. Xue, Pattern formation in a predator-prey model with spatial effect. *Physica A* **391** (2012) 5987–5996.
[43] Y.A. Kuznetsov, Elements of Applied Bifurcation Theory, 2nd edn. Applied Mathematical Sciences, Vol. 112. Springer, New York, NY (1998).
[44] K. Manna and M. Banerjee, Stationary, non-stationary and invasive patterns for a prey–predator system with additive Allee effect in prey growth. *Ecol. Complex.* **36** (2018) 206–217.
[45] J. Shen and Y.M. Jung, Geometric and stochastic analysis of reaction–diffusion patterns. *Int. J. Pure Appl. Math.* **19** (2005) 195–244.
[46] L.N. Guin and H. Baek, Comparative analysis between prey-dependent and ratio-dependent predator-prey systems relating patterning phenomenon. *Math. Comput. Simul.* **146** (2018) 100–117.
[47] A. Calbet and M.R. Landry, Phytoplankton growth, microzooplankton grazing, and carbon cycling in marine systems. *Limnol. Oceanogr.* **49** (2004) 51–57.
[48] R.W. Eppley, Temperature and phytoplankton growth in the sea. *Fishery Bull.* **70** (1972) 1063–1085.
[49] J.E. Bissinger, D.J.S. Montagnes, J. Sharples and D. Atkinson, Predicting marine phytoplankton maximum growth rates from temperature: improving on the Eppley curve using quantile regression. *Limnol. Oceanogr.* **53** (2008) 487–493.
[50] Q.P. Li, P.J.S. Franks and M.R. Landry, Microzooplankton grazing dynamics: parameterizing grazing models with dilution experiment data from the California Current Ecosystem. *Mar. Ecol. Progr. Ser.* **438** (2011) 59–69.
[51] J.R. Beddington, Mutual interference between parasites or predators and its effect on searching efficiency. *J. Anim. Ecol.* **44** (1975) 331–340.
[52] D. Straile, Gross growth efficiencies of protozoan and metazoan zooplankton and their dependence on food concentration, predator–prey weight ratio, and taxonomic group. *Limnol. Oceanogr.* **42** (1997) 1375–1385.
[53] L.D.J. Kuijper, T.R. Anderson and S.A.L.M. Kooijman, C and N gross growth efficiencies of copepod egg production studied using a dynamic energy budget model. *J. Plankton Res.* **26** (2004) 213–226.
[54] Y. Olsen, T. Andersen, I. Gismervik and O. Vadstein, Protozoan and metazoan zooplankton-mediated carbon flows in nutrient-enriched coastal planktonic communities. *Mar. Ecol. Progr. Ser.* **331** (2007) 67–83.
[55] A.G. Hirst and T. Kiørboe, Mortality of marine planktonic copepods: global rates and patterns. *Mar. Ecol. Progr. Ser.* **230** (2002) 195–209.
[56] A. Okubo, Oceanic diffusion diagrams. *Deep-Sea Res.* **18** (1971) 789–802.
[57] J.A. MacKinnon and M.C. Gregg, Spring mixing: turbulence and internal waves during restratification on the New England Shelf. *J. Phys. Oceanogr.* **35** (2005) 2425–2443.